

Turnstile area as a measure for chaotic transport in magnetic confinement fusion devices

C. B. smiet,¹ L. Rais,¹ J. Loizu,¹ and R. Davies²

¹*Ecole Polytechnique Fédérale de Lausanne (EPFL), Swiss Plasma Center (SPC), CH-1015 Lausanne, Switzerland*

²*Max Planck Institute for Plasma Physics, Wendelsteinstraße 1, 17491 Greifswald*

(*Electronic mail: christopher.smiet@epfl.ch.)

(Dated: 21 March 2025)

We analyze stochasticity in the magnetic fields of magnetic confinement fusion reactors by calculating the lobe areas of turnstiles - a method developed for characterizing transport into and out of resonance zones in Hamiltonian dynamical systems. We develop an efficient algorithm based on an action principle to calculate this quantity directly from the magnetic field, including stellarator magnetic fields which are sourced by a complicated set of three-dimensional coils. In the analyzed devices, the turnstile area on the inboard (plasma-facing) manifolds is much smaller than the turnstile area on the outboard (wall-facing) manifolds. The application of the turnstile area calculation for the design of future reactors will be discussed.

Magnetic confinement fusion reactors confine the charged particles of a plasma by channeling them along the twisting field lines of a magnetic field. A magnetic confinement fusion reactor is designed such that in the center, magnetic field lines lie neatly on nested toroidal surfaces; providing good confinement, but at the edge of the plasma the field is designed with features that guide the plasma to specific locations on the wall. The features of the magnetic field that are created at the plasma edge have direct analogies to Hamiltonian Dynamical systems: in a Tokamak a hyperbolic trajectory (x-point) is placed that separates a region of closed trajectories, and guides plasma to the wall along its stable and unstable manifolds. In a stellarator one designs a resonance (magnetic island) at the edge of a region of closed trajectories (plasma region), to control the location where the plasma interfaces with the vessel wall, or one intentionally creates a region of chaotic field lines. In all currently investigated magnetic confinement fusion devices, transport of plasma particles and heat to the wall is partially determined by transport through a homo- or heteroclinic connection at the edge. Transport through such a barrier is quantified by the area of a region of phase space (an amount of magnetic flux) called the 'turnstile' that under the Hamiltonian flow (field line following) is mapped in or out of the resonance zone (plasma region). In this paper we lift methods to determine this phase-space transport, and apply them to the analysis of the magnetic field in the edge fusion reactors. We demonstrate this method on two-dimensional fast-evaluating maps, on a toy model of a tokamak discharge, and calculate this measure of transport in several stellarator configurations, including configurations of the existing device W7-X. Calculating this transport is important for understanding current and planned fusion reactors, and can be potentially used to control the field structure in the edge as we design future devices.

I. INTRODUCTION

Magnetic confinement fusion has the goal to generate energy through the fusion isotopes of hydrogen, by heating a plasma confined in a strong magnetic field created by a set of coils. The coils are arranged around a toroidal volume, in which field lines lie on nested surfaces (magnetic surfaces). The charged particles of the plasma are, to lowest order, confined to move along the field lines (integral curves of this field), as their perpendicular motion is constrained through the Lorentz force. Because of this, the effective transport of heat and particles along the field lines is up to ten orders of magnitude higher along the field lines than perpendicular to the field lines, and temperature and pressure are nearly constant on magnetic surfaces.

A good way to understand the particle and heat transport in a fusion reactor is therefore to inspect the trajectories of magnetic field lines. To do this one constructs a Poincaré section, by choosing a cross-section of the torus and recording all the points at which a field line intersects that plane. Such a Poincaré section is shown in figure 1 for the W7-X stellarator. The trajectories colored in red form the plasma region, where field lines lie on nested magnetic surfaces. At the very center of this foliation is a single field line, called the *magnetic axis*, named because it is often used as the axis of a toroidal coordinate system. The magnetic axis is a curve that closes on itself after one toroidal turn (long way around the torus). The ratio of the number of times a field line winds around the magnetic axis to the number complete transits of the fusion device is called the *rotational transform* ι . In tokamaks, which are axisymmetric, it is conventional to use the inverse, called the *safety factor* $q = 1/\iota$.

Figure 1 shows two different configurations that can be achieved in W7-X, the top half shows the standard configuration, the bottom half shows the GYM00+1750 configuration achieved by running different currents through the coils. The trajectories colored in blue form surfaces that do not enclose the magnetic axis, and structures like this are called a *magnetic island*. These can form on surfaces that have a rational $\iota = m/n$ where m is the number of times field lines on that

surface wind around the axis and n the number of full toroidal transits around the device the field line makes to achieve this. In the standard configuration (top half figure 1) the island chain in the edge has $\iota = 1$ and consists of 5 islands, and is called a 5/5 island chain. In the GYM00+1750 (bottom panel figure 1) the rotational transform in the edge is higher and $\iota = 5/4$. At the center of the islands is a field line that closes on itself, and this is called the island *o-point*. In between the *o*-points the island regions approach each other, and there is another field line that closes on itself called the island *x-point*.

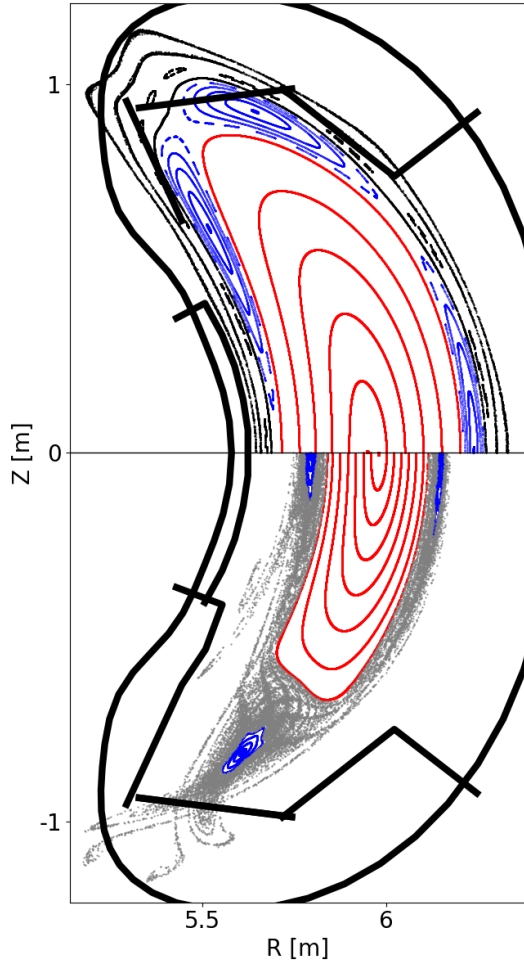


FIG. 1. Poincaré section of the magnetic field in the W7-X stellarator. (top): Standard configuration and (bottom): GYM00+1750 configuration with chaotic field lines. Field lines in the core are colored red, field lines in the island divertor are colored blue, and field lines outside of the divertor are colored black and field lines that follow chaotic trajectories are colored grey. The plasma facing components and vessel wall are shown in thick black lines.

W7-X has been designed to have this island chain in the edge, to form what is called an (island) *divertor*, which creates spatial separation between the plasma facing components and the plasma itself. The wall is also shown in figure 1 with black lines. Since the field lines in the island connect regions close to the plasma with the outboard side of the island, heat and particles flowing along them can be quickly transported

away from the plasma. Conditions along the divertor path (the path the plasma takes from the core to the wall) can be controlled and optimized such that much of the heat is dissipated through recombination and radiation, which minimizes damage to the wall.

Another interesting possibility for the magnetic field topology in the edge of stellarators is the *nonresonant divertor*^{1,2}, in which the central region of nested surfaces is not bounded by a clearly identifiable island chain. Instead the field transitions from nested surfaces to a region of stochastic field lines. Theoretical investigations show that transport through chaotic regions is very important for their operation³. Nonresonant divertors are actively being investigated in current experiments⁴ and considered for future devices⁵.

Under suitable conditions^{6,7}, the dynamics of magnetic field line flow can be reduced to a $1\frac{1}{2}$ -dimensional Hamiltonian dynamical system (though this can break down^{8,9}). This equivalence has been recognized very early on in the development of fusion theory, and guided much of the nomenclature in the field. A magnetic island is often called a ‘resonance’, tokamaks have Resonant Magnetic Perturbation (RMP) coils that can create islands or disturb the nested surfaces.

There is a vast body of work studying transport in chaotic systems coming from the Hamiltonian dynamical systems’ literature, that can explain a wide-ranging list of physical phenomena. The first step in this regard was the frightening observation by Poincaré that three-body systems such as the earth’s orbit around the sun perturbed by Jupiter are generally chaotic¹⁰. These fears were laid to rest by theories by Kolmogorov, Arnol’d¹¹ and Moser¹², proving that invariant orbits persist under small perturbations, providing barriers to the dynamics. The rate of transport through such a barrier when it breaks up can explain the ionization probability of atoms in microwave fields¹³. The probability of passing from one region of phase space to another can also be used to calculate probability of ship capsizing^{14,15}.

In this paper we focus on a specific quantity that captures the amount of trajectories that pass into and out of a resonance in a dynamical system, called the *turnstile* (also sometimes called a ‘lobe dynamics’). This analysis was developed independently by MacKay, Meiss and Percival¹⁶ and Benmion and Kadanoff¹⁷. This metric is especially relevant for the magnetic fields in fusion, as the transport into- and out of resonances (the magnetic islands in the edge) directly affects the fusion reactor divertor. We analyze this quantity directly in fusion-relevant fields, and develop an algorithm based on an action principle to efficiently calculate this quantity in the magnetic fields of fusion devices.

Whilst the literature on transport in Hamiltonian dynamical systems is often formulated in terms of differential forms, or otherwise in ways that are agnostic to the dimensionality of the Hamiltonian system under consideration, in this paper we strictly limit ourselves to $1\frac{1}{2}$ -dimensional Hamiltonian systems and two-dimensional sections. This will make the exposition simpler to follow for plasma physicists wishing to apply this understanding to the fields in fusion reactors.

This paper is organized as follows: In section II we first describe three types of maps that have been used to describe

fusion-relevant fields: iterated maps, perturbed toy models which describe Tokamaks, and the three-dimensional stellarator fields generated by coils. In section III we discuss fixed points of the field line map and we describe an algorithm to find them in any map. In section IV we analyze a specific two-dimensional iterated map, calculate the slow- and fast *manifolds* of several resonances in it, and illustrate how the turnstile mechanism leads to transport in- and out of a resonance zone. We also describe an algorithm to locate *hetero-* or *homoclinic* orbits in such maps. In section V we develop a toy model describing an axisymmetric tokamak-like magnetic field, and apply perturbations to it. We describe the calculation of the turnstile area based on an action principle, and use it to calculate how the turnstile area changes with perturbation strength. In section VI we apply this to the three-dimensional fields produced by optimized coils of stellarators. We analyze two configurations from the open-source QUASR database, that exhibit very different field structures in the edge. We also analyze a chaotic configuration of the W7-X stellarator called the GYM00+1750 configuration. Section VII concludes with discussion of the competition between chaotic transport in the field and other transport processes, and an outlook for designing future divertors.

II. ITERATED MAPS, TOY MODELS, AND THREE-DIMENSIONAL FIELDS

An essential tool for studying dynamical systems is the Poincaré section; the return map from a section transverse to the dynamics to itself¹⁰. We can study such maps in three different ways; the simplest is through *iterated maps*, fast-evaluating functions on our space. Second one can use a *toy model*, that describes a Hamiltonian-like function from which a field and perturbations to it are generated. Lastly we will consider fully three-dimensional fields that are generated by coils embedded in space. In this section we will briefly describe these three types of maps.

A. iterated maps

It has long been recognized that the magnetic connectivity in fusion devices can be understood through the study of two-dimensional measure-preserving iterated maps, starting with the seminal paper by John Greene¹⁸. In these maps the difficult and computationally costly task of integrating trajectories (following field lines) is replaced by fast-evaluating analytical expressions of two variables¹⁹.

One of the most well-studied and famous iterated maps is the Chirikov-Taylor standard map²⁰, the study of which led Chirikov to formulate the *overlap criterion* determining when the combination of different perturbations leads to chaos. It has also been used to define the residue criterion²¹, a highly accurate method to define the break up of strongly irrational KAM (Kolmogorov, Arnol'd, Moser) surfaces, and to show that after such a surface breaks up, transport through the surface is still hindered by a broken invariant set with the struc-

ture of a cantor set, or a *cantorus*²². All these results have had profound impact on the understanding of the magnetic field in fusion reactors.

The standard map is an example of a *twist map*, which equates to fusion magnetic fields where the twist of the field lines of each surface (i.e., the rotational transform ι) is monotonic.²³ Aubry²⁴-Mather²⁵ theory applies to twist maps and proves (amongst others) that periodic orbits are related to extrema of an action. Fusion fields however can and sometimes do violate the twist condition, and these can be studied by *nontwist maps*^{6,26}. These maps also find application in describing particle transport in the fast-particle trajectories²⁷ (a Hamiltonian system that is different from, though related to the one describing field line flow).

In Section IV we will analyze an iterated map called the *tokamap* specifically designed for creating maps that are similar to the field line structure in fusion devices²⁸.

B. Perturbed toy models

A next step in complexity comes when we consider fields, and the maps that they generate, that are provided by analytical expressions. There are many different ways to mathematically represent such fields, but a good approach is to start with a formulation that guarantees integrability of the field, and add perturbations to it.

One approach is to exploit the connection to Hamiltonian systems directly, and analytically describe a Hamiltonian. Through a coordinate transformation to a suitable three-dimensional space we get our magnetic field. For example, Punjabi and Boozer have analyzed trajectories Hamiltonian systems that describe a nonresonant divertor¹, and show chaotic mixing of trajectories just around the last closed surface, with several locations where the trajectories quickly leave the system, i.e. are diverted^{2,29}. The locations where the field lines are diverted have been found to be caused by fixed points (see section III)⁹.

Another method is to describe a simple axisymmetric field, on which we apply perturbations. In axisymmetry (using cylindrical (R, ϕ, Z) coordinates) one can construct a flux function $\Psi(R, Z)$, and a separate function describing the toroidal field. The poloidal components of the field (defined as the components perpendicular to the ϕ -direction) are defined by treating Ψ as a stream function. Although it is easy to identify the Hamiltonian for such fields, this is not often done. This representation is ubiquitous in tokamak equilibrium reconstruction, where the problem of finding the right flux function can be quickly solved from diagnostic data.

By construction, the field lines lie on the contours of the flux function, and there is no chaos. We can break the axisymmetry by further adding ϕ -dependent fields, to have a versatile toy model where the interaction of several symmetry-breaking modes can be studied.

The trajectories are calculated by evaluating this field and integrating curves. The Poincaré map $f(R, Z)$ is calculated by

tracing field lines:

$$f_i^n(R, Z) = \int_{\phi_0}^{\phi_0 + n2\pi} B^i(R, \phi, Z) / B^\phi(R, \phi, Z) d\phi \quad (1)$$

where $i \in \{R, Z\}$, and integration is performed over toroidal angle ϕ for a full period, and the superscript n determines how many times around the torus a field line is traced for.

In section V we will develop such a toy model, and analyze the field line flow in it. We will use the versatility of this model to analyze different perturbations.

C. Maps defined by three-dimensional fields

The methods developed with the iterated maps and the toy model will allow us to analyze chaotic transport in the magnetic fields of actual stellarator fusion reactors. In a stellarator, the magnetic field is generated by a complicated set of coils $\{\mathcal{C}_i\}$, and the magnetic field generated by these is calculated from the Biot-Savart law:

$$\mathbf{B}(\mathbf{r}) = \frac{\mu_0}{4\pi} \sum_i \oint_{\mathcal{C}_i} \frac{j_i d\mathbf{l} \times \mathbf{r}'}{|\mathbf{r}'|^3} \quad (2)$$

where j_i is the current carried by coil \mathcal{C}_i , and \mathbf{r} the point in three dimensions where the field is evaluated, \mathbf{r}' is the vector between \mathbf{r} and the point on the coil. Evaluating the Biot-Savart integral is computationally very costly and calculating the field line map can take a significant amount of time per trajectory.

Stellarators are often designed with *stellarator symmetry* and multiple *field periods* n_{fp} . This means that there are only a few unique coils that are translated and rotated in space, such that the field repeats itself toroidally with period $T = 2\pi/n_{fp}$. This means that the field line map can be evaluated more efficiently by only integrating over a single period:

$$f_i^n(R, Z) = \int_{\phi_0}^{\phi_0 + nT} B^i / B^\phi d\phi \quad (3)$$

where T is the repetition period in the field.

We note that equation (3) requires that $B^\phi < 0$ everywhere (or $B^\phi > 0$). The fields defined by a finite set of coils, e.g. equation (2) do not necessarily fulfil this requirement, and in a given section there can exist field lines that do flow around the torus, but for example get caught close to a coil. This means that the field line map cannot be defined at every point of $(R, Z) \in (\mathbb{R}^+ \times \mathbb{R})$, but we must restrict the field line map to a region⁹, called the *maximal mappable region*.

In section VIA we will analyze the chaotic fields in several configurations from the open-source QUASR repository^{30,31} and analyze the transport in a chaotic configurations of the W7-X fusion reactor.

III. THE FIELD LINE MAP AND IT'S FIXED POINTS AND MANIFOLDS.

In this section we discuss fixed points of the field line map. We demonstrate an algorithm to find them, and discuss the

different types of fixed points. We also define the *stable manifold* and *unstable manifold* that are associated with hyperbolic fixed points.

A fixed point of the field line n -map is a point where $f^n(R, Z) = (R, Z)$. The existence of at least one fixed points is guaranteed by Brouwers' fixed point theorem³², assuming that there is at least some region that maps wholly onto itself. Given that the goal of a magnetic confinement fusion reactor is to generate a field where field lines foliate nested toroidal surfaces (invariant tori), this is a necessary condition for the fields under consideration. The 'magnetic axis', the field line that lies at the center of this foliation of magnetic surfaces, is a fixed point of the field line map.

A. locating fixed points

Fixed points can be located using a Newton's method. To first order, using the linearized map around a point \mathbf{x} the field line map can be approximated as:

$$f^n(\mathbf{x} + \delta\mathbf{x}) \approx f^n(\mathbf{x}) + M\delta\mathbf{x} \quad (4)$$

where the matrix M (with indices $M_{ij} = \partial_j f_i^n$, the labels i, j run over the dimensions R and Z) is the Jacobian matrix of the field line map. M is a 2×2 matrix with real coefficients. From this, we can solve for which step $\delta\mathbf{x}$ the linear approximation brings us to a fixed point, i.e. $f(\mathbf{x} + \delta\mathbf{x}) = \mathbf{x} + \delta\mathbf{x}$:

$$\mathbf{x} + \delta\mathbf{x} = f^n(\mathbf{x}) + M\delta\mathbf{x} \implies \quad (5)$$

$$M\delta\mathbf{x} - \mathbb{I}\delta\mathbf{x} = \mathbf{x} - f(\mathbf{x}). \quad (6)$$

Thus a series of points is defined by the relation:

$$\mathbf{x}_{k+1} = \mathbf{x}_k + (M - \mathbb{I})^{-1}(\mathbf{x} - f(\mathbf{x}_k)). \quad (7)$$

This series rapidly converges in the vicinity of a fixed point, but as any Newton method it can take wild steps far away from fixed points.

For iterated maps (sec 2A), the Jacobian is easily evaluated by differentiating the mapping function, but for integrated maps (sec. 2B and 2C) we must differentiate the result of integrating field lines. Luckily this can be efficiently calculated by differentiating equation (3):

$$\partial_j f_i^n = \int_{\phi_{hi0}}^{\phi_0 + nT} \partial_j \frac{B^i}{B^\phi} d\phi = \int_{\phi_{hi0}}^{\phi_0 + nT} \frac{\partial_j B^i}{B^\phi} - \frac{B^i}{(B^\phi)^2} \partial_j B^\phi d\phi \quad (8)$$

starting with initial value $\partial_j f_i^{n=0} = \mathbb{I}$, and where the trajectory of integration is determined by the field line itself, equation (3).

The above calculations are numerically implemented in the *pyoculus* package³³, freely available on Github.

B. properties of fixed points

The Jacobian of the field line map M defined in equation (4) describes the structure of the map around fixed points. The

Poincaré map must be measure preserving, which at a fixed point means that $\text{Det}(M) = 1$. Hence $M \in \text{SL}_2(\mathbb{R})$, the special linear group of order 2 over the reals^{34,35}.

The structure of $\text{SL}_2(\mathbb{R})$ is well known³⁶, and consists of three subsets that act as distinct linear transformations of the plane:

- elliptic elements: Points around the fixed point are mapped on trajectories that form invariant ellipses.
- parabolic elements: shear mappings, where the point is part of a line of points that are fixed, and points on either side of the line are mapped in opposite directions.
- hyperbolic elements: points in the vicinity of the fixed point are mapped along hyperbolic trajectories.

Points where $\text{Tr}(M) > 2$ are hyperbolic elements. The eigenvalues of the matrix M (solutions to the characteristic equation $\lambda_{\pm} = (\text{Tr}(M) \pm \sqrt{\text{Tr}(M)^2 - 4})/2$) are both real and positive, and because $\text{Det}(M) = 1 \implies \lambda_1 \lambda_2 = 1$ we can say without loss of generality $\lambda_1 > 1$ and $\lambda_2 < 1$. The eigenvector corresponding to λ_1 we call \mathbf{v}_1 or the *unstable eigenvector*, and the eigenvector corresponding to λ_2 we call \mathbf{v}_2 , or the *stable eigenvector*. By equation (4) the eigenvectors correspond with directions relative to the fixed point in which points are mapped further away from, respectively closer to the fixed point. This defines the two asymptotic directions that give nearby trajectories a characteristic x-shape and in fusion literature such points are called x-points (elliptic points conversely are called o-points).

The set of all trajectories that asymptotically approach a hyperbolic point ($\{\mathbf{x} | \lim_{m \rightarrow \infty} f^m(\mathbf{x}) = \mathbf{x}_0\}$) are called the *stable manifold*. In the linear region around the fixed point (where eq. (4) holds), the manifold is the span of \mathbf{v}_2 , as the less-than-unity eigenvalue implies that points get mapped closer, but the manifold extends much further as will be discussed in the next section. The set of trajectories that asymptotically leave the fixed point, or conversely, whose limit $\{\mathbf{x} | \lim_{m \rightarrow -\infty} f^m(\mathbf{x}) = \mathbf{x}_0\}$ are called the *unstable manifold*, which starts off in the linear regime as the span of \mathbf{v}_1 .

IV. ITERATED TWO-DIMENSIONAL MAPS: CALCULATING MANIFOLDS.

In this section we will use two-dimensional iterated maps to illustrate the stable and unstable manifold, and transport through a resonance zone. We will use the Tokamap, a class of maps developed specifically to describe fusion magnetic fields²⁸. First we will describe the map itself and how it is calculated. Next we will locate fixed points of this map, and the manifolds associated with them. Finally we will describe how the intersections of these manifolds determine transport through the system via the ‘turnstile’ mechanism.

The Tokamap has the form:

$$f(\psi_v, \vartheta_v) = (\psi_{v+1}, \vartheta_{v+1}) \quad (9)$$

$$\psi_{v+1} = \frac{1}{2} \left[P(\psi_v, \vartheta_v) + \sqrt{P(\psi_v, \vartheta_v)^2 + 4\psi_v} \right], \quad (10)$$

$$\vartheta_{v+1} = \vartheta_v + W(\psi_{v+1}) - \frac{K}{(2\pi)^2} \frac{1}{(1 + \psi_{v+1})^2} \cos(2\pi\vartheta_v). \quad (11)$$

Where K is a parameter determining a perturbation strength. P is given by:

$$P(\psi_v, \vartheta_v) = \psi_v - 1 - \frac{K}{2\pi} \sin(2\pi\vartheta_v) \quad (12)$$

and $W(\psi_{v+1})$ determines the winding of the trajectories (the change in ϑ at a given ψ , which in the unperturbed case corresponds to the rotational transform of the field lines). We choose a monotonically increasing W given by:

$$W(\psi) = \frac{w_0}{4} (2 - \psi)(2 - 2\psi + \psi^2). \quad (13)$$

W has a minimum value of w_0 at ψ_0 . The parameters ψ and ϑ are easily identifiable with the variables to describe fusion fields: respectively, the flux label ψ_p , which acts as a radial coordinate, and the poloidal angle θ . Tokamaps have the desirable property that no trajectories pass through the line $\psi = 0$, which in fusion devices corresponds to the magnetic axis.

We have plotted trajectories of the Tokamap in figure 2, with the values $K = 4.7$ and $w_0 = 0.9$. In the vicinity of $\psi = 0$ there is a region where trajectories close in ϑ , corresponding to closed magnetic surfaces. The trajectories are given a gradient in color starting with yellow at $\psi = 0$ and $\vartheta = 0.5$ to dark blue at $\psi = 0.43$, $\vartheta = 0$. At larger ψ , we see trajectories that do not close in ϑ , but form several discrete circles. These trajectories are analogous to magnetic islands. The stochasticity in the field increases until a large period 3 island chain is seen, which forms the boundary to a completely stochastic field in which a period 5 island chain and a period 2 island chain are seen.

In such a stochastic region, trajectories explore large portions of ψ , as is seen from the mixing of different colored trajectories. This can have the effect of mixing between hot and cold regions in the plasma which is detrimental to confinement. Even though there is mixing, we still see the gradient of color from red to blue in the stochastic region, and one can ask the question which fraction of the field lines near the plasma will reach regions further out, and how many iterations of the map this will on average take.

Such questions are important for designing a fusion reactor, because the hot plasma is confined by the magnetic field, and heat and particle transport along the field lines can be up to 10 orders of magnitude faster along the field, the trajectories of the system than perpendicular to them. If we place a wall around the plasma, where do the trajectories intersect the wall, on average how far along the trajectory (how many iterations

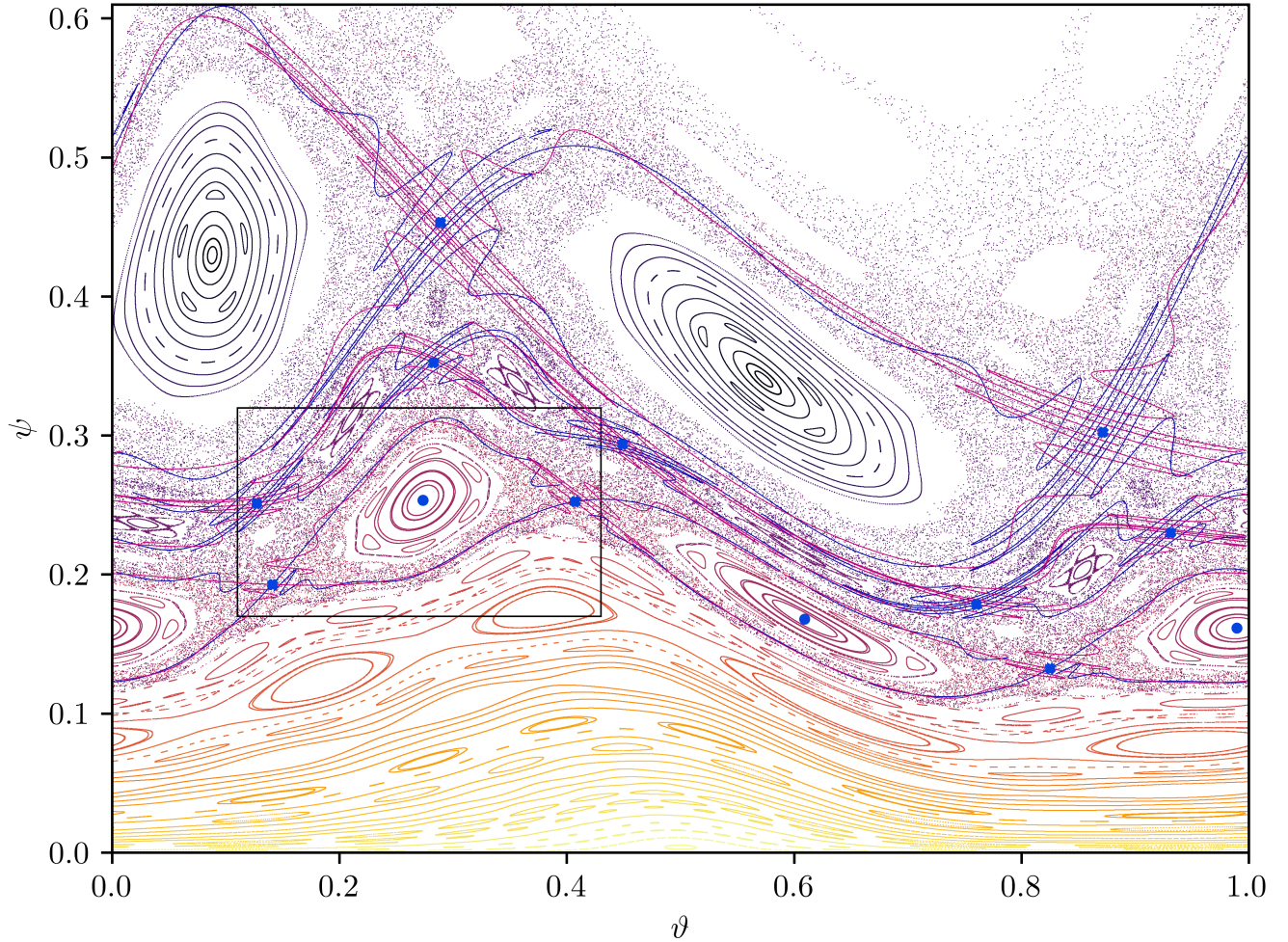


FIG. 2. Trajectories of a Tokamak configuration, showing an inner region of mostly closed surfaces, bordered by a stochastic region in which transport is determined by field structures surrounding large resonances. 80 trajectories are followed for 4000 iterations each. The unstable fixed points in the $1/3$, $2/5$ and $1/2$ island are shown in blue, and their stable manifolds are shown in blue, their unstable manifolds are shown in magenta. The stable (unstable) manifolds associated with these fixed points are shown in magenta (blue)

of the map) does it take for the plasma to reach the wall- these are questions that require knowledge of the magnetic topology.

For this, we first calculate the fixed points of each of the island chains. For the period 3 island chain, we use the Newton's method in equation (7) applied to the 3-map. We find an elliptic period-3 orbit in the center of the island, shown with a blue dot in figure 2, and a hyperbolic period-3 orbit in between marked with a blue x. Similarly we find the x-points in the period 5 and period 2 orbits.

We calculate the manifolds of all hyperbolic points. First we choose one of the n points of the periodic orbit, and evaluate the linearized mapping M and its eigenvectors. We choose point a distance of 10^{-5} (using the Euclidean norm on ψ, ϑ) from the fixed point along the unstable eigenvector, and evaluate the map of that point. After confirming that this is in the linear regime, we choose 50 points logarithmically spaced between the initial point and the mapped to point. We then

calculate the trajectories of these 50 distinct points for 12 applications of the n -map (12 was found to be a sufficient number to illustrate the manifold). If \mathbf{v} is an unstable eigenvector of M , then $-\mathbf{v}$ is as well, so we calculate the second unstable manifold as well. Since the first point of this segment of points maps to the last, the result is a continuous line, that starts straight but becomes more convoluted upon higher iterates of the map. The result of this calculation are the unstable manifolds of the x-points, shown in magenta.

We calculate the stable manifolds similarly using the stable eigenvector and the backwards map. This results in the blue lines shown in figure 2.

In order to understand the chaotic transport of field lines through an island chain, we take a zoomed-in look at a single island indicated by the box in figure 2. Figure 3 shows the two period-3 fixed points labeled \mathbf{x}_0^1 and \mathbf{x}_0^2 and the stable and unstable manifolds associated with them. The area around the island o-point, and bounded by the manifolds, is called the *is-*

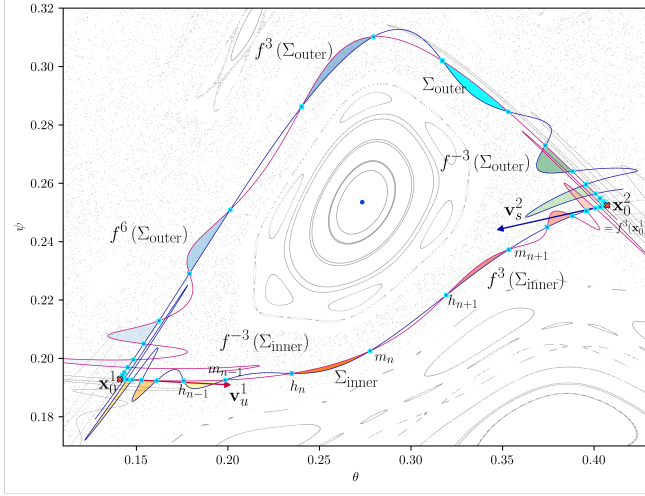


FIG. 3. Illustration of transport through the barrier created by the first period 3 island chain in the Tokamap. Trajectories enter the zone around the island through a ‘turnstile’ created by the intersecting manifolds on the inner heteroclinic connection. The orange set originates from the plasma region (yellow areas), and is mapped forwards into the region around the island (red areas). There is an equivalent set that is mapped from the island zone into the plasma zone. The transport away from the island is governed by another turnstile illustrated with the cyan area, whose backwards map is shown in green, and forwards map in blue.

land resonance zone (for the exact definition see³⁷). Consider the orange area labeled Σ_{inner} , on the bottom, defined by the intersections of the inner manifolds. If we apply the forwards map $f^{3n}(\Sigma_{\text{inner}})$, it is mapped to the red areas, and when we apply the backwards map, it is mapped to the yellow areas.

It is clear to see that the yellow area starts outside of the resonance zone, but upon several mappings it becomes the red area, which is clearly inside the resonance zone. There is an identical area that is mapped from inside the resonance zone out. Because this acts like a ‘gate’ that exchanges a fixed amount of trajectories upon each mapping, it is called the *turnstile* after the gates that limit the flux of persons in and out of buildings. See Meiss³⁷ for a more detailed explanation.

Once a trajectory has entered the resonance zone through the inner turnstile, if it is to pass out of it again, and reach the chaotic region beyond the island chain, it must again pass through a turnstile, this time defined by the intersections of the outer manifolds. This is indicated with the progression from green via cyan to blue. If a divertor is placed intersecting the resonance zone, transport from the plasma to this divertor is determined predominantly by the *turnstile area* on the inner connection.

The two manifolds intersect each other along two trajectories which are called the *heteroclinic orbits*. Since they are in both the unstable manifold of fixed point 1, and the stable manifold of fixed point 2, $\lim_{n \rightarrow \infty} f^n = \mathbf{x}_0^1$ and $\lim_{n \rightarrow -\infty} f^n = \mathbf{x}_0^2$. These orbits must be located in order to define the sections of the manifold that bound a turnstile lobe.

A. locating homo- and heteroclinic orbits

Locating the heteroclinic orbits can be done by computing the complete manifolds, and locating their intersections. Calculating the manifolds is a computationally costly endeavor, as it requires integrating a large number of trajectories for many iterations. For iterated maps this is not an issue, but if the map is calculated by the numerical integration of trajectories, the computational cost can be significant. Therefore, we implement an algorithm to find these heteroclinic orbits directly with many fewer required integrations.

We locate a heteroclinic trajectory that starts at \mathbf{x}_0^1 , and has its limit at \mathbf{x}_0^2 , as illustrated in figure 3. To calculate the heteroclinic trajectory of the inner manifolds, we must integrate along the unstable manifold from \mathbf{x}_0^1 , and along the stable of \mathbf{x}_0^2 . To locate this trajectory, we start with a random point in the linear regime along the unstable eigenvector (defined in sec. III) of fixed point 1,

$$\mathbf{x}_u = \mathbf{x}_0^1 + \varepsilon_u \cdot \mathbf{v}_u^1 \quad (14)$$

(here the superscript denotes the fixed point label). We choose ε small enough to be in the linear regime, here 10^{-6} , and we then compute $f^{m \cdot n_{\text{map}}}(\mathbf{x}_u)$, where $m = 3$ is the order of the fixed point, and n_{map} is the number of times this initial point is mapped back to the same intersection.

Next we choose a similar point in the stable manifold of fixed point 2:

$$\mathbf{x}_s = \mathbf{x}_0^2 + \varepsilon_s \cdot \mathbf{v}_s^2 \quad (15)$$

and calculate $f^{-m \cdot n_{\text{map}}}(\mathbf{x}_s)$.

If \mathbf{x}_s and \mathbf{x}_u are heteroclinic points, then $f^{m \cdot n_{\text{map}}}(\mathbf{x}_u) = f^{-m \cdot n_{\text{map}}}(\mathbf{x}_s)$, but this is unlikely to be the case. We therefore minimize the components of:

$$\Delta = f^{m \cdot n_{\text{map}}}(\mathbf{x}_0^1 + \varepsilon_u \cdot \mathbf{v}_u^1) - f^{-m \cdot n_{\text{map}}}(\mathbf{x}_0^2 + \varepsilon_s \cdot \mathbf{v}_s^2). \quad (16)$$

This gives a system with two variables (ε_s and ε_u) and two constraints (Δ_ψ and Δ_θ), which is solved using a standard root-finding method *hybrj* implemented in *scipy*.

We choose $n_{\text{map}} = 8$ for both the stable and the unstable manifold integration, and the values of $\varepsilon_{s,u}$ are initially set to 10^{-6} . The root-finding converges resulting in a heteroclinic trajectory with 16 points. These are shown in the top panel of 2.

The heteroclinic trajectories thus found are shown in figure 3 as the blue circles (squares) for the minimizing (minimax) orbits respectively.

The turnstiles appear at the intersection between stable and unstable manifolds. In the case above, these manifolds originated from different fixed points, but it is equally possible to perform the calculations on manifolds that originate from the same fixed point. In that case we are considering an *homoclinic* intersection, and the trajectories are called *homoclinic* trajectories. The method of locating homoclinic points is identical if $\mathbf{x}_0^1 = \mathbf{x}_0^2$.

V. CHAOTIC TRANSPORT IN A PERTURBED TOKAMAK

In this section, we will analyze chaotic transport in a tokamak-like field that has been perturbed. We will first describe the analytical expressions used to calculate an axisymmetric, tokamak-like field and analytical perturbations to it. We calculate the manifolds in this perturbed system and describe an algorithm to find the homoclinic orbits, the intersections of these manifolds. Using the homoclinic orbits, we describe an efficient algorithm to calculate the turnstile area using an action principle by MacKay, Meiss and Persival¹⁶.

In a three-dimensional field, the fast-evaluating function such as (9), is replaced by an expensive integration of the trajectory as in (1). Though the variables (ψ, ϑ) are replaced with (R, Z) , all of the discussed algorithms remain the same. We will start with a axisymmetric field, that resembles the configuration in a Tokamak. Calculation of the manifolds in tokamak geometry has been studied theoretically by Punjabi and Boozer³, Wei and Liang³⁸, and their signatures have been shown in experiments³⁹. Here we build upon this work by implementing our efficient method of calculating the turnstile area, and hence a measure for the degree of stochasticity and stochastic transport.

We create an analytical toy model that resembles the field in a Tokamak fusion reactor. A general expression for such a field is:

$$\mathbf{B}_{\text{circular}} = \frac{1}{R} \frac{\partial \psi}{\partial Z} \hat{R} + \frac{1}{R} \frac{\partial \psi}{\partial R} \hat{Z} + B^\phi \hat{\phi} \quad (17)$$

Where ψ is a flux surface label, and is related to the ϕ component of the vector potential through $\psi = R^2 A^\phi$. We choose ψ such that the field lies on concentric nested circular tori centered on (R_0, Z_0) :

$$\psi(R, Z) = (R - R_0)^2 + (Z - Z_0)^2 = \rho^2 \quad (18)$$

And define our toroidal field as:

$$B^\phi = 2\sqrt{R^2 - \rho^2}(q_a + \frac{s}{2}\rho^2)/R^2 \quad (19)$$

which is chosen such as to give a simple expression for the rotational transform i or it's inverse, $q = 1/i$ which is more often used in tokamak physics:

$$\frac{1}{i(\rho)} = q(\rho) = q_a + \frac{s}{2}\rho^2. \quad (20)$$

The toroidal field B^ϕ (eq. (19)) is written in terms of a vector potential which is given in the appendix.

In a tokamak, a hyperbolic point is created by a circular separatrix coil underneath or above (or both) the plasma, carrying a current in the same direction as the plasma current. We calculate this field using the analytical expressions for a circular current loop given in⁴⁰. The vector potential for such a loop with radius R_l and positioned horizontally at $Z = Z_l$ is given by:

$$\frac{\mu_0}{4\pi} \frac{4IR_l}{\beta R} \left(\frac{(2 - k^2)K(k^2) - 2E(k^2)}{k^2} \right). \quad (21)$$

Here K and E the complete elliptic integral of the first and second kind respectively, $\alpha^2 = (R_l - R)^2 + (Z - Z_l)^2$, $\beta^2 = (R_l + R)^2 + (Z - Z_l)^2$, and $k = 1 - \alpha^2/\beta^2$.

Equations (17) and (21) are implemented numerically in terms of their respective vector potentials, and the magnetic field is calculated through $\mathbf{B} = \nabla \times \mathbf{A}$ using automatic differentiation provided by JAX⁴¹. We choose $R_0 = 6$, $q_a = 1.16$, $s = 1.2$ for the axisymmetric field, and for the separatrix coil we choose $R_l = 6$, $Z_l = -5.5$, $I = 10\pi/\mu_0$. The resultant field is integrated numerically, and a Poincaré section is shown in figure 4 a). The fixed points of the 1-map of this field are also located, and these are the magnetic axis shown with a blue dot, the location of the separatrix coil shown with a red square, and a hyperbolic x-point in between, shown with an orange cross.

Because the fields given by equations (17) and (21) are axisymmetric, the resultant Poincaré section in fig. 4 a) does not exhibit any chaos, and there are no turnstiles. Now we add a perturbation that depends on the toroidal angle ϕ with the form:

$$A_{\text{pert}}^\phi = f(\rho) \cos(n\phi + \phi_0) \cos(m\theta + \theta_0) \quad (22)$$

where ϕ is the usual toroidal angle and θ is the poloidal angle; $\tan(\theta) = (Z - Z_0)/(R - R_0)$ (with (R_0, Z_0) the location of the magnetic axis, blue circle in fig. 4 a)). The radial distribution $f(\rho)$ of the perturbation can have any form, we choose one that places the perturbation smoothly everywhere in the configuration by using a Maxwell-Boltzmann probability density function with distribution parameter d :

$$f(\rho, d) = \frac{\sqrt{2}}{\sqrt{\pi}} \frac{\rho^2}{d^3} \exp \frac{-\rho^2}{2d^2} \quad (23)$$

From this we calculate

$$\mathbf{B}_{\text{pert}} = \nabla \times \mathbf{A}_{\text{pert}} \quad (24)$$

\mathbf{B}_{pert} lies in the R, Z -plane, and is tangent to contours of constant $R^2 A_{\text{pert}}^\phi$. The perturbation field oscillates m times in one R, Z -plane, and this pattern rotates n times as the angle goes from 0 to 2π . We choose $\phi_0 = 0$, $\theta_0 = 0$, distribution width $d = 2$, and mode numbers $m = 6$ and $n = 1$. This is shown in figure 4.

When this perturbation is applied, the field becomes stochastic, as is seen in figure 4 (right). Islands have opened up on several magnetic surfaces, and the region around the separatrix surface has become chaotic. The x-point is no longer clearly visible in the Poincaré section. Nevertheless, the fixed point is still there, and it is found using the Newton method described in section III A, and it is indicated with a orange cross.

In section IV we considered a *heteroclinic* intersection, where stable manifolds of one fixed point intersect with the unstable manifolds of a second point in the same orbit, but here, we can consider the simpler where the stable and unstable manifolds originate from the same point; a *homoclinic* connection. We find the homoclinic trajectory in this integrated map using the same algorithm as described in IV A, and calculate the manifolds in the same way as described in section IV. The results of this calculation are shown in figure 4 b).

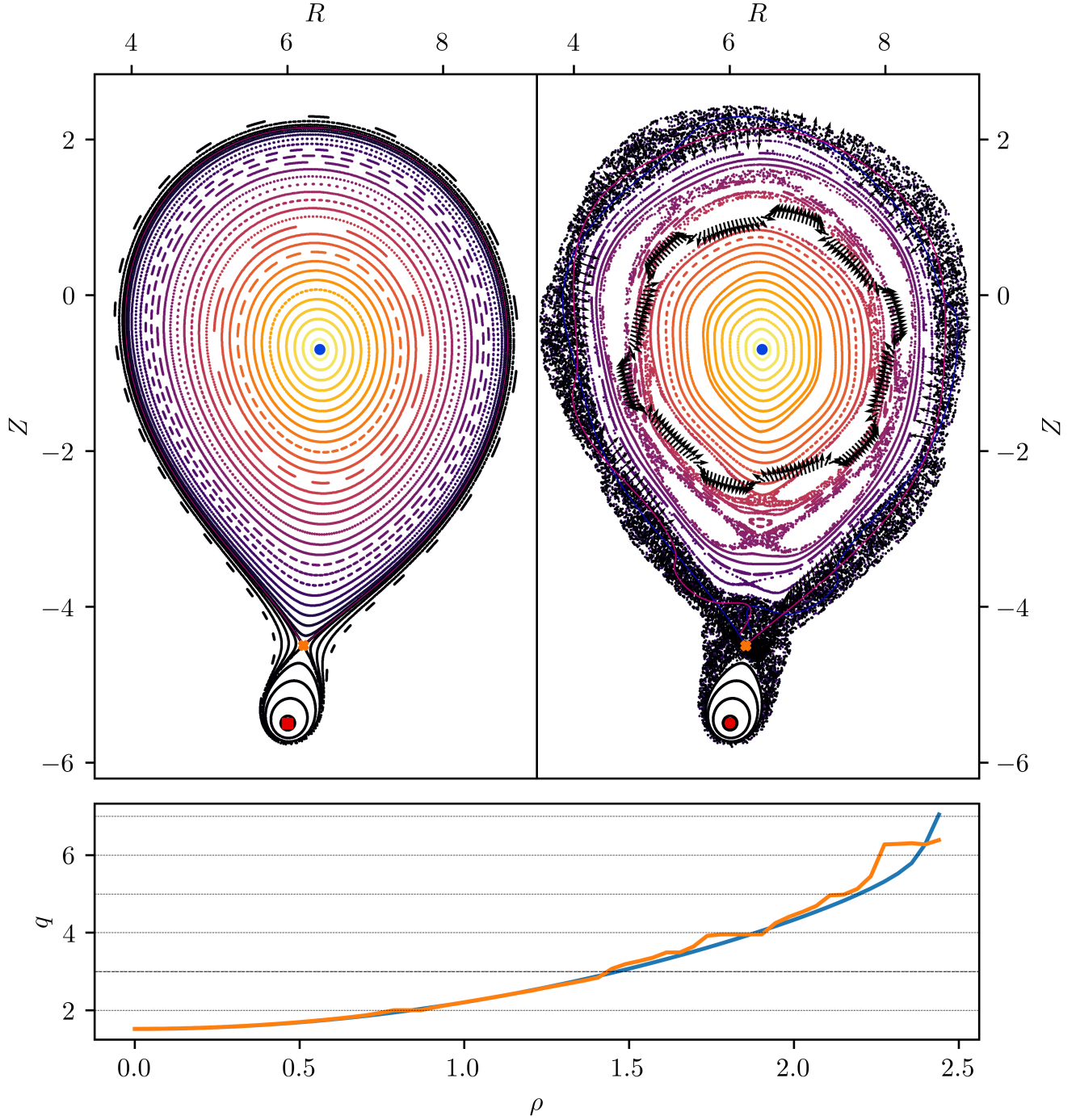


FIG. 4. Poincaré section of the axisymmetric analytical field and the result of applying a perturbation. a) Axisymmetric field \mathbf{B}_{axi} with the o-point of the main plasma in blue, the separatrix coil location indicated in red, and the x-point it creates identified by an orange cross. The unstable and stable manifolds that enclose the plasma overlap, and are shown by a magenta and blue line respectively. b) Effect of applying a $m = 6, n = 1$ perturbation field. The direction the perturbation field is indicated by arrows located on the unperturbed separatrix and on a circle in the plasma region. The perturbation creates islands inside the plasma region, and stochastization around the separatrix. The stable and unstable manifolds (magenta and blue respectively) no longer overlap. c) safety factor q (inverse of rotational transform i measured along a horizontal line from the axis, in both the unperturbed (blue) and perturbed field (orange). The islands in the perturbed field correspond with the regions of flat q at integer values of q .

A. Turnstile area calculation

We will now describe an efficient algorithm to calculate the turnstile flux $\Sigma_{\text{turnstile}}$. One could do this by calculating the shape of the manifold between the two homoclinic orbits, and integrating $\oint \mathbf{A} \cdot d\mathbf{l}$ over this boundary. This approach is used in numerical solvers such as *lober*¹⁵.

Macay, Meiss, and Percival¹⁶ describe a simpler method to calculate the turnstile area. Here we give a brief overview of that method, but for a full description and definitions of terms, we refer the reader to the review by Meiss³⁷. Their method is based on the Lagrangian form λ calculated on homoclinic orbits. They show that if the map is exact, $\lambda = F(x, x')$ (where x is a point in the section and x' is the point mapped to) which is one of the standard generating functions for canonical transformations. They go on to show, for a homo (or hetero)clinic connection, which has two homo (hetero)clinic trajectories, m_t the minimax orbit and h_t the minimizing orbit, that the homoclinic lobe area can be calculated directly from:

$$\Sigma_{\text{turnstile}} = \sum_{t=-\infty}^{t=\infty} (\lambda(m_t) - \lambda(h_t)) \quad (25)$$

In the case of magnetic fields, the Lagrangian form is calculated by integrating the vector potential along the field line [THIS IS NOT EXACTLY RIGHT]:

$$\lambda(m_t) = \int_0^{mT} \mathbf{A}(\mathbf{x}) \cdot d\mathbf{l}. \quad (26)$$

where the integration is started at $\mathbf{x} = m_{t-1}$ and the integration is performed along the field line.

It seems rather remarkable that the computation of a complicated area in phase space can be performed by the simple summation (equation (25)) of integrals (equation (26)). Though the formulation in terms of Lagrangian forms and area forms holds in any dimension, in the case of a three-dimensional flow and a two-dimensional map, this formula has an intuitive explanation.

Figure 5 illustrates how the calculation of the turnstile lobe can be understood. To calculate the flux through the dark shaded area, which without loss of generality we label the n -th occurrence of the lobe, one can use Stokes' theorem and integrate the vector potential A over γ_n , a section of the unstable manifold, and τ_n , a section of the stable manifold:

$$\Sigma_{\text{turnstile}} = \int_{\tau_n} \mathbf{A} \cdot d\mathbf{l} + \int_{\gamma_n} \mathbf{A} \cdot d\mathbf{l} \quad (27)$$

We can now shift the integral over the unstable manifold by transporting it along the field to the next intersection. This integral now becomes:

$$\Sigma_{\text{turnstile}} = \int_{\tau_n} \mathbf{A} \cdot d\mathbf{l} + \int_{\xi_{n-1}} \mathbf{A} \cdot d\mathbf{l} + \int_{\gamma_{n-1}} \mathbf{A} \cdot d\mathbf{l} - \int_{\zeta_{n-1}} \mathbf{A} \cdot d\mathbf{l} \quad (28)$$

$$= \int_{\gamma_1} \mathbf{A} \cdot d\mathbf{l} + \lambda(m_n) + \int_{\gamma_1} \mathbf{A} \cdot d\mathbf{l} - \lambda(h_n). \quad (29)$$

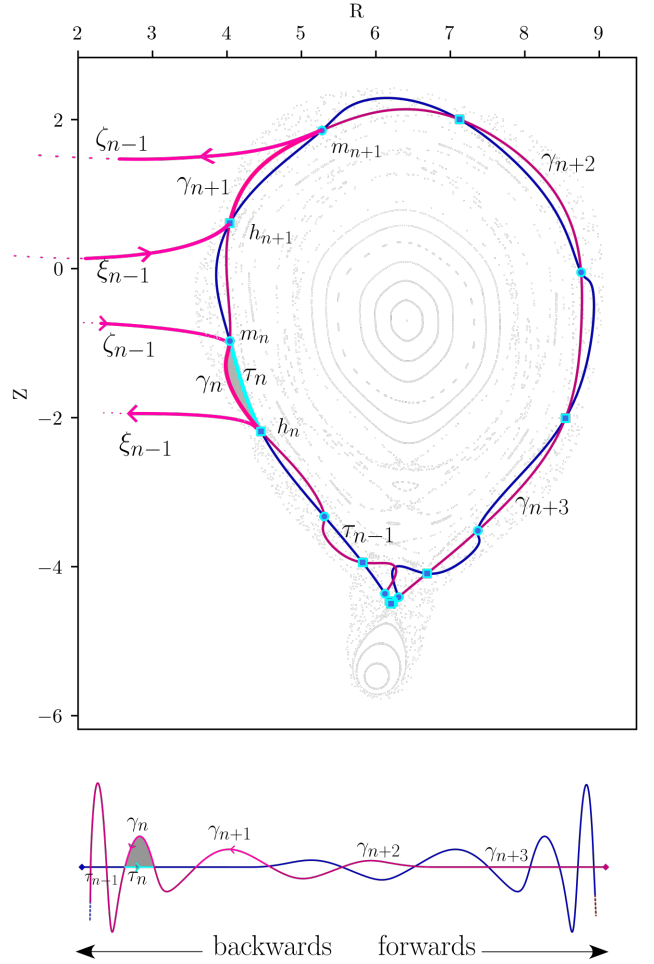


FIG. 5. Illustration of the calculation of a turnstile area. The area Σ_n shown in gray is bounded by turnstile sections γ_n and τ_n between homoclinic points, is given by the integral of the vector potential over the curve $\tau_n \cup \gamma_n$. This integral can be modified to run over $\tau_n \cup \xi_{n-1} \cup \gamma_{n-1} \cup \zeta_n - 1$. This can be repeated until γ_{n-i} is in the linear regime of the fixed point. Similarly the integration over τ_n can be moved forward to τ_{n+j} in the linear regime of the slow manifold. (bottom): illustration of the turnstile area calculation where the intersecting manifolds have been laid flat.

We can repeat this process, shifting the integration over the stable manifold to γ_{n+2} , γ_{n+3} , etc, until it is so close to the fixed point that it tends to zero, and all that is left is a sum over the action integrals.

We do the same with the integral over the stable manifold section τ_n , replacing it with action integrals moving it to the section connecting τ_{n+1} , τ_{n+2} and so forth, until also this contribution shrinks, and we are left with equation (26).

Instead of integrating the vector potential over two curve segments, whose geometry has to be found by integrating many trajectories, we can instead identify two specific trajectories along which to integrate the vector potential. One issue in the practical application of equation (26) is when to terminate the sum. In practice only about $N = 10-20$ applications of the map suffice to bring a point from the linear regime

of the unstable manifold into the linear regime of the stable manifold. Increasing the number of points in the homoclinic trajectories will make the sum converge, but at a large computational cost. Instead, when we are in the linear regime, we can close the sum by evaluating $\int \mathbf{A} \cdot d\mathbf{l}$ along the straight line connecting the last homoclinic points.

We now use this algorithm to compare the effects of varying the perturbation mode numbers and perturbation amplitude on the turnstile area in the tokamak toy model equilibrium. To compare different perturbations, we normalize the perturbation strength the axisymmetric field strength, by evaluating the maximum of $|B_{\text{pert}}|/|B_{\text{axi}}|$ on the unperturbed separatrix. Poincaré sections at three amplitudes, for the mode numbers $m = 2, 4, 7, 9$ (n always 1) are shown in figure 6 a). All perturbations create chaotic regions, but the perturbations with lower m create more stochasticity in the core. The rotational transform crosses the rational values $m/1$ for those $m < 7$ and the mode couples with resonant surfaces there.

The size of the turnstile area as a function of the mode number is shown in figure 6 b). The area scales approximately linearly with the applied perturbation, though some modes show nonlinearity at high amplitudes. The method is able to calculate turnstile areas over a large range of perturbation amplitudes, and at the maximum applied perturbations the perturbation field is a significant fraction of the unperturbed field strength. We thus have a reliable method to evaluate the turnstile area over a broad range of perturbation amplitudes, from nearly integrable fields, to moderately chaotic fields up to almost completely stochastic fields.

Different perturbations are more or less effective at creating stochastic transport on the separatrix. To compare this, we plot the turnstile area at a fixed perturbation amplitude of $\max\left(\frac{|B_{\text{pert}}|}{|B_{\text{axi}}|}\right) = 0.0040$ for all different modes. This is shown in figure 6 n).

Understanding which modes are most effective at creating stochasticity in fields is an important and long-standing area of research in tokamak physics, where so-called Resonant Magnetic Perturbation (RMP)⁴² coils are placed around the vessel to create a stochastic edge. Computing the lobe structures is key to predicting the heat footprints on divertor targets⁴³. We expect that the turnstile area calculation could be an effective tool in designing RMP fields. Given the potential risk posed by runaway electrons for future experiments, there is a big effort in studying mitigation methods, and one proposal are Passive Runaway Electron Mitigation Coil (PREMCs)⁴⁴. Here a shaped coil is placed near the vessel, and the current induced in it by the abrupt changes in flux brought on by the disruptive events preceding the formation of a dangerous beam of near-relativistic electrons, will induce a current in the coil which stochasticizes the field, disrupting the beam. Such a coil could be optimized to create maximum stochasticity at desired locations.

VI. TRANSPORT IN THE STELLARATOR EDGE

We finally turn our attention again to stellarator fields, and in this section we will analyze magnetic island structures occurring at the edge of stellarator configurations. We will first analyze two configurations from the QUASR database^{30,31} of stellarator configurations. We will use these configurations to verify the turnstile area calculation. We show that in general, the turnstile areas are larger on the outside (coil-facing) manifolds, and smaller on the inside (plasma-facing) side. Finally we will analyze a specific configuration of the W7-X stellarator called GYM+1750, and show how the structures in the connection length are caused by the manifolds.

Whereas the toy model fields were given by analytical expressions, the fields in stellarators are generated by a set of coils. The coils are modeled as current-carrying filaments from which the field is calculated using the Biot-Savart integral. The coils can be represented in different ways, but we use any of representations provided by the `simsopt`⁴⁵ stellarator optimization suite which are based on a Fourier representation to describe the curve. See the documentation of `simsopt` for the implementations. `simsopt` also contains optimized routines to evaluate the Biot-Savart integral (equation (2)) and vector potential, as well as derivatives thereof. `pyoculus` has been augmented with an interface to `simsopt`, such that the field generated by the coils can be used in equation (3) to define the field line map.

A. Turnstile area in fields from the QUASR database

The QUASR database contains roughly 300,000 quasisymmetric stellarator configurations^{30,31}. These configurations each consist of a set of coils and currents that have been optimized to produce a vacuum magnetic field that has been optimized to confine particles through quasisymmetry^{46,47}. The entire database can be browsed interactively <https://quasr.flatironinstitute.org/>, and contains configurations with different numbers of coils, field periods and types of symmetry. The coils can be downloaded in the format used by `simsopt`.

We focus on one specific QUASR configuration with identifier 242612, which is a four field period device with only eight coils in total. The rotational transform starts below 1, and monotonically increases to a value of around 1 at the edge. We plot the coils and the field strength a surface of the configuration in Figure 7 a-b). The coils are indicated with gray curves, and a magnetic surface of the configuration is shown, colored by the magnitude of the magnetic field on the surface.

The Poincaré section of the field, shown in figure 7 (c), shows a few islands in the core, and a large 4/4 island chain at the edge, which is surrounded by a stochastic region. This stellarator configuration thus resembles a conventional stellarator with an island divertor like W7-X, except optimized for quasisymmetry instead of quasi-omnigenity. One interesting feature of this configuration is that the resonance in the edge has itself bifurcated, resulting in two elliptic fixed points

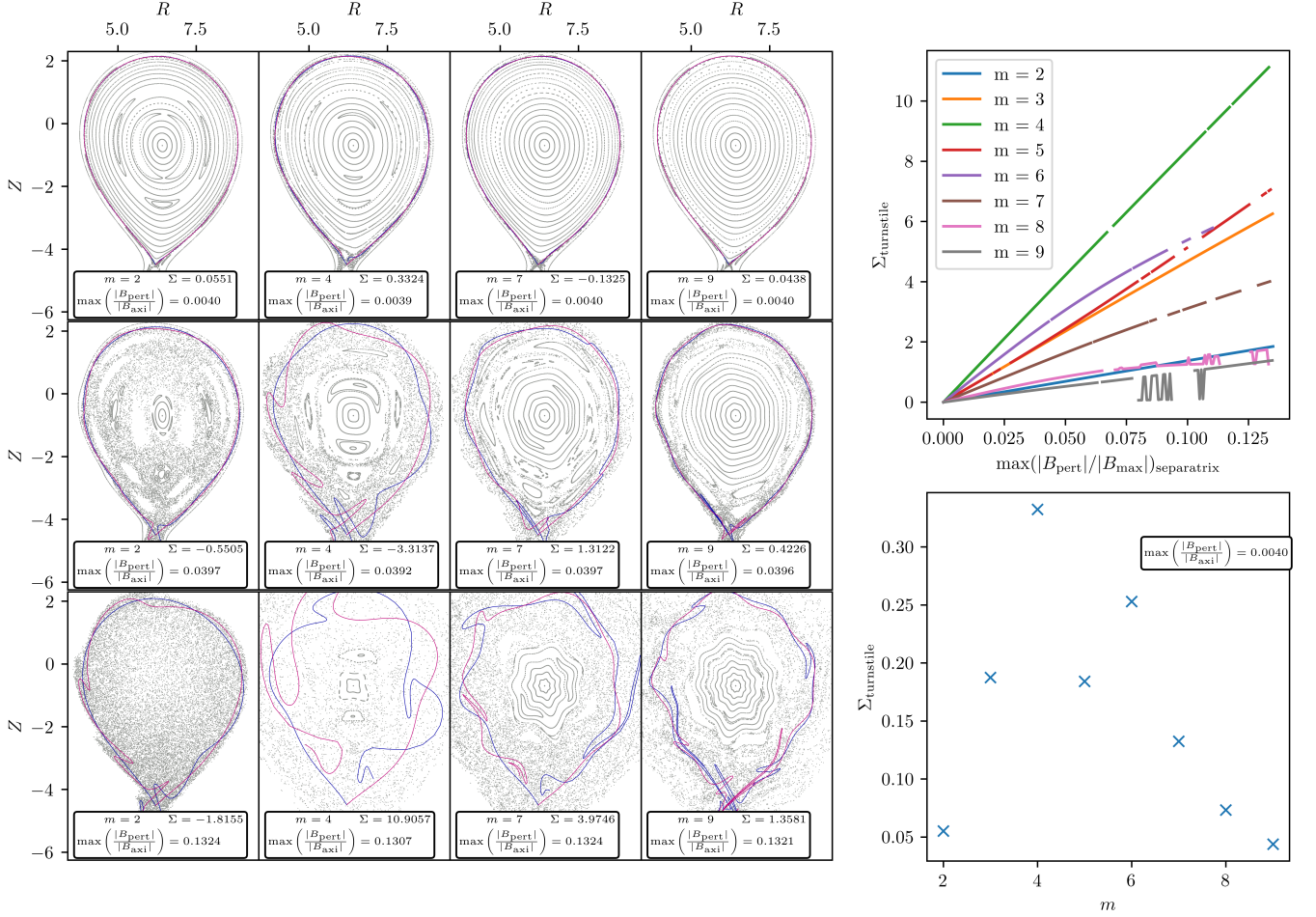


FIG. 6. The effect of perturbations on the turnstile area using the same axisymmetric field as in figure 4. a-l: Each column has a different poloidal mode number m , and each row has a different amplitude of the perturbation. Different mode numbers affect the field and chaotic transport differently. Low m mode numbers are resonant with the surfaces inside, and create stochastic fields throughout the volume. m: Turnstile area vs perturbation amplitude. The response to perturbation is mostly linear, but can act nonlinearly at very high amplitudes. n: Turnstile area at a perturbation amplitude of 0.004. Certain modes are more efficient at increasing turnstile area and generating stochastic transport than others.

Manifold	Turnstile Area (in)	Turnstile Area (out)
xp9manifold	6.3879e-12	3.7425e-12
outermanifold	9.1613e-07	3.4471e-05
islandmanifold	1.3626e-06	1.3627e-06

TABLE I. Turnstile areas of select resonances in the QUASR 242612 configuration.

shown in light and dark green, and a hyperbolic point in between.

We calculate the manifolds, heteroclinic points, and turnstiles for both the inner and outer heteroclinic connections in the 9/10 and 4/4 resonances, as well as the period four homoclinic connections (left and right). The results of this are presented in table I

B. Turnstile area calculation verification

We verify the turnstile area calculation using the field of the QUASR 242612 configuration and the manifold on the outer heteroclinic connection of the 4/4 outermost resonance zone. First we calculate the area using a simple triangle approximation, by approximating the turnstile lobe with a simple triangle. The chosen triangle does not exactly match the lobe, but it is chosen such that it roughly agrees. This very crude approximation is shown with the solid black lines in figure 8, and the triangle has a basis length of $b = 0.02312m$, and a height of $h = 0.00651m$ resulting in an area of $7.5264 \cdot 10^{-5} m^2$.

We next use a more robust method, where we actually resolve the turnstile lobe using 40 trajectories logarithmically spaced between the heteroclinic orbits. We calculate the area using Gauss's area formula (also known as the shoelace algorithm) which gives the area enclosed by a polygon determined

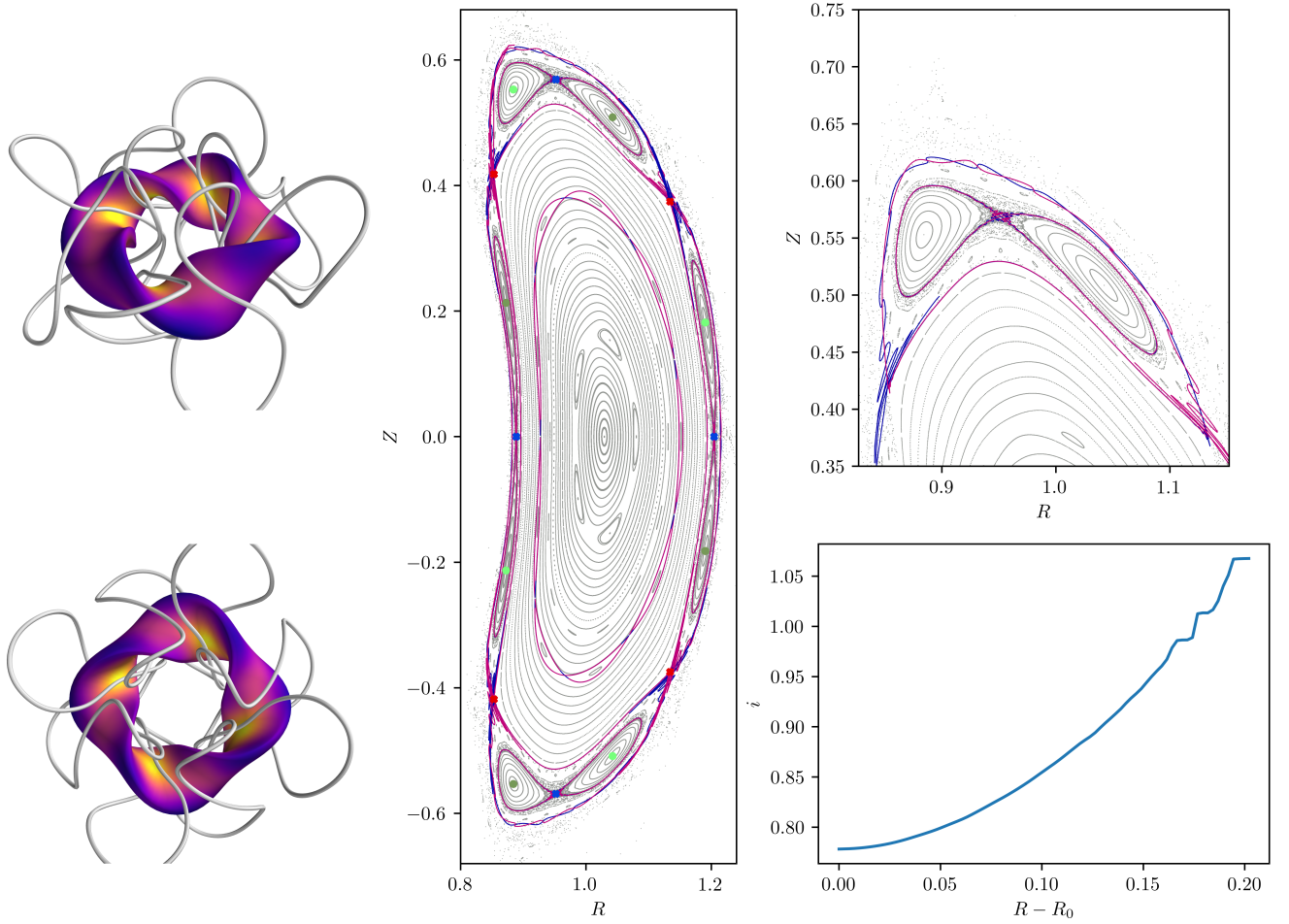


FIG. 7. Analysis of QUASR configuration 242612. a, b: Coils and a magnetic surface of the configuration colored by the magnetic field strength. c: Poincaré section at $\phi = 0$ plane, including the manifolds of the 9/10 island chain and the outer 4/4 island chain, as well as manifolds around the hyperbolic point inside of the 4/4 island chain. d: zoom in of the turnstiles around the edge 4/4 island. e: rotational transform profile calculated along the midplane.

by points x_i, y_i by:

$$\Sigma = \frac{1}{2} \sum_{i=1}^n y_i (x_{i-1} - x_{i+1}) \quad (30)$$

This robust method is also used in the code `lober`¹⁵ to evaluate lobe areas. The result of this calculation is shown in table II.

The turnstile calculation returns the amount of flux through the lobe in $[Tm^2]$. In order to get an area, we divide by the field strength in the lobe. We evaluate the toroidal field at the geometrical center of the lobe points, indicated with the red dot in figure 8. The field strength here is 0.4759, resulting in a very similar area.

The last verification that we do is to directly calculate $\oint_{\text{lobe}} \mathbf{A} \cdot d\mathbf{l}$ over the boundary of the lobe by a simple Riemannian sum over the segments of the lobes.

The four different calculations show good correspondence, with the crude triangle approximation of course being the least accurate.

C. QUASR 229079

We next analyze the structures in the edge of QUASR configuration 229079. This is a three field-period quasi axisymmetric stellarator with 18 coils and a low rotational transform. The coils and a flux surface of this configuration are shown in figure 9. This configuration is rather compact, and has strongly shaped ridges on the inboard side of the tori which create rotational transform, very similar to the configurations generated by Plunk⁴⁸ through a perturbative modification of axisymmetric equilibria. Configurations such as this, though not explicitly optimized for, are common in the QUASR database among the high aspect-ratio low rotational transform configurations. Henneberg and Plunk⁴⁹ have investigated the potential of such configurations as a reactor dubbed the 'Compact Stellarator-Tokamak hybrid'.

In the Poincaré plot of this configuration we see, towards the edge a few islands, starting with the 3/7 and the 6/15, and then the first resonance for which we analyze the turnstiles

triangle area [m^2]	Shoelace area [m^2]	$\Sigma_{\text{turnstile}} [m^2 \cdot T]$	$\Sigma_{\text{turnstile}}/B_{\text{center}}^\phi$	$\oint_{\text{boundary}} \mathbf{A} \cdot d\mathbf{l}$
7.5264e-05	7.2437e-05	3.4471e-05	7.2436e-05	3.4444e-05

TABLE II. The turnstile area of the outer heteroclinic connection in the QUASR 242612 stellarator calculated by four different methods.

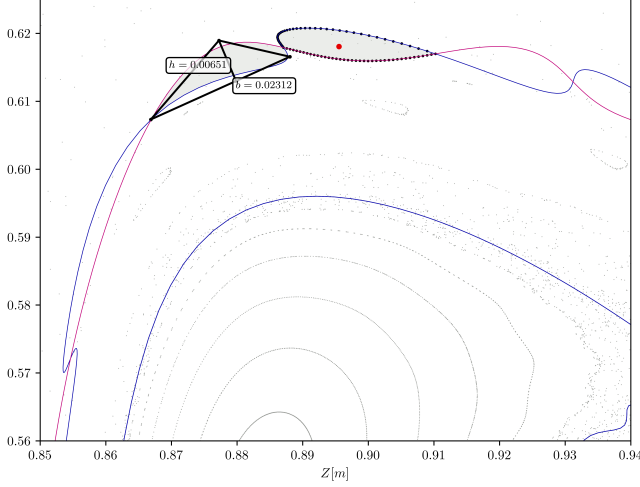


FIG. 8. Verification of the action-principle based turnstile area computation against geometrical and direct computation. The triangle used for approximating the area is shown in black lines, the points used for calculating the area and integral of the vector potential are shown on the right lobe.

is the resonance on the $3/8$ island, which is period-doubled and shows a $6/16$ island chain. In such a case, the rational surface has broken into two separate islands, and we plot the stable (unstable) manifolds surrounding the first island with lavender (purple), the stable (unstable) manifolds around the second with light blue (blue). In such a period-doubled case, the turnstiles around one island chain can be much larger than those around the other.

The $6/16$ island chain marks one of the last occurrences of clear surfaces surrounding the plasma, what follows is a very large region of stochastic magnetic field. In this region many resonances can be found, of which we show the $3/9$, $3/10$, $3/11$ in different colors.

Figure 7 d shows a zoom in to these manifolds, with only one occurrence of each colored. We see the size of the manifold with respect to the size of the resonance zone increase significantly from each resonance zone to the next. This is quantified in table III. The size of the island even becomes significant with respect to the size of the resonance zone, and we even see a large fraction of overlap between the manifolds of the $3/10$ and $3/11$ resonances.

The rotational transform profile is calculated by integrating over 40 field periods, and fitting the rotation angle. This is shown in figure 9 d). This is not a perfect measure for rotational transform, but the profile does show that the configuration crosses the $1/4$ resonance twice, and in the Poincaré plot we do find two $3/12$ resonances the outer one is shown with pink markers at the very edge of the configuration. This in-

Manifold	Turnstile Area (in)	Turnstile Area (out)
manifold8a	$5.8090e-07$	$2.5502e-06$
manifold8b	$5.2863e-10$	$4.4831e-10$
manifold9	$3.6184e-05$	$7.3541e-05$
manifold10	$1.3430e-04$	$2.1494e-04$
manifold11	$2.5547e-04$	$3.7709e-04$

TABLE III. Turnstile areas of select resonances in the QUASR 229079 configuration.

icates that there are nontwist map dynamics²⁶ at play in this outermost stochastic region.

D. Turnstile area in the chaotic low-iota configurations in the W7-X stellarator

Finally we will use the tools to calculate the turnstile area in configurations of the Wendelstein 7-X (W7-X) stellarator. W7-X was optimized for neoclassical transport and low bootstrap current. It is therefore said to be a quasi-isodynamic stellarator. W7-X has already shattered the records for stellarator field accuracy⁵⁰, fusion triple product⁵¹, and confinement⁵².

W7-X is a five field period device that creates the magnetic field with a total of 70 main coils⁵³ that generate the field. Per half-field period, there are 5 unique *modular* coils, that have complicated shapes and two *planar* coils. The coil configuration and the shape for the plasma region is shown in figure 10 b. These are copied around the device according to stellarator symmetry and field periodicity to produce the full coil set. The power supplies to these superconducting coils are connected according to this symmetry, but the current in each of these 7 unique coil groups can be set separately.

When the modular coils carry their design current of 1.62 MA each, and there is no current in the planar coils, the stellarator generates the *standard configuration*. This configuration has a large volume of closed flux surfaces, that is terminated with a large $5/5$ island chain that acts as a divertor and determines the strikepoints of the plasma on the wall (and the location of heat loading).

One of the design goals for W7-X was also its versatility as a research reactor, and different configurations can be achieved by changing the currents in the coils. The strongly shaped modular coils create the intricately shaped and twisted magnetic field, whereas the modular coils are so oriented as to provide a field along the axis without any additional shaping. By running a current to the planar coils which opposes the toroidal field, an increase of twist is achieved resulting in a configuration with higher rotational transform.

When the current in the modular coils is set to $I_{\text{modular}} = 1.1095\text{MA}$, and the current in the planar coils is $I_{\text{planar}} = -\frac{1}{3}I_{\text{modular}} \simeq -0.3661\text{MA}$, we get a configuration where the

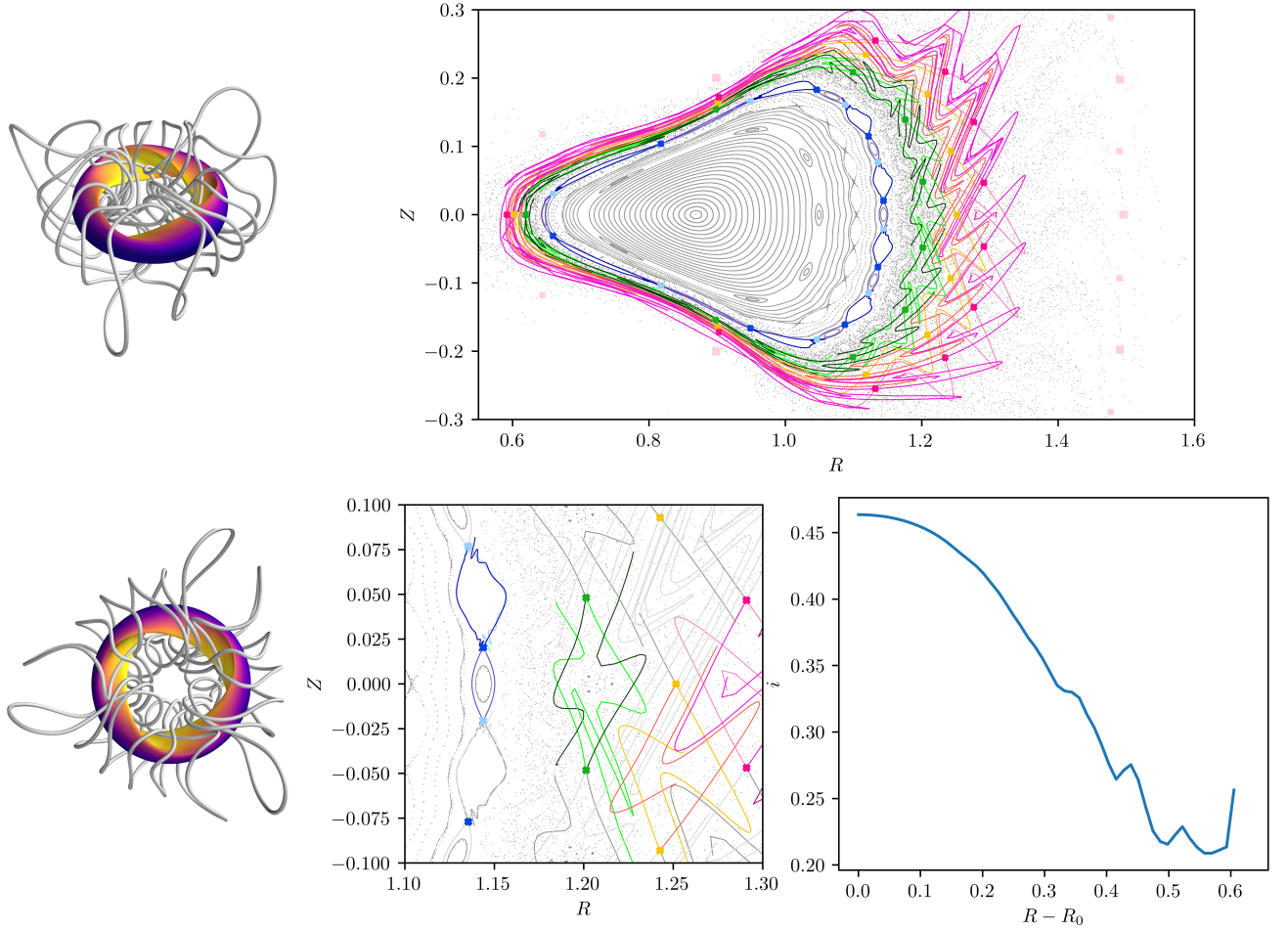


FIG. 9. Analysis of QUASR configuration 229097. a, b: Coils and a magnetic surface of the configuration colored by the magnetic field strength. c: Poincaré section at $\phi = 0$ plane, showing an ordered center surrounded by a large stochastic region that contains many high-order resonances. The manifolds associated with the 6/16 (light blue/blue and violet/purple), 3/9 (light-/dark green), 3/10 (yellow/orange), and 3/11 (pink/fuchsia) are shown, as well as the fixed points of a 3/12 chain in pink. c: zoom in of the interacting turnstiles in the chaotic edge, with only the manifolds around a single island resonance zone colored. d: rotational transform profile calculated along the midplane.

rotational transform in the edge is $1\frac{1}{4}$. A Poincaré section of this field is shown in figure 10 d, and the resultant rotational transform profile is shown in figure 10 c. This configuration is called GYM00+1750. One of the interesting features of this configuration is that the edge of the field is chaotic, which has led to it's study in the context of nonresonant divertors^{2,9}.

One method that is often employed to design divertors is to analyze the connection length in the divertor region, with tools such as EMC3-EIRENE. The EMC3-Lite code is capable of calculating heat loads on plasma-facing components (PFCs) and PFC-to-PFC connection lengths for a given magnetic field and PFC arrangement⁵⁴. For both, it relies on following Monte Carlo particles (which either simply follow magnetic field lines or take a random walk to imitate anisotropic diffusion), which are tracked on a field-aligned grid (for more details on the grid scheme see⁵⁵). The PFC-to-PFC connection length L_c is specific to each field line and is not recorded, but the grid cell-averaged connection length $\langle L_c \rangle$ is calculated and recorded, and is useful for revealing the structure of

the magnetic field and predicting regions of heat loading on PFCs (see for example^{54,56}). $\langle L_c \rangle$ is calculated by tracing Monte Carlo particles both forwards and backwards along the field until they intersect a PFC. The connection length of this field line contributes to all grid cells it passes through, and $\langle L_c \rangle$ for a given cell is the arithmetic mean of L_c of all unique field lines passing through the cell. The cell in which each magnetic field line is initialised is selected to ensure that each cell contains at least n_{\min} unique trajectories. The location of an initialised field line in a cell is uniformly random. An upper cutoff $L_{c,\max}$ is applied to each field line, since field lines which do not intersect a PFC (intact surfaces around island O-points, for example) would otherwise be traced indefinitely. In the result presented here we select $n_{\min} = 100$ and $L_{c,\max} = 10^4$ meters. The grid resolution used here is 480 points in the radial direction and 1025 points in the poloidal direction. This is several times larger than is typically required for heat deposition calculations but is used here to show the fine structure emerging from the magnetic chaos.

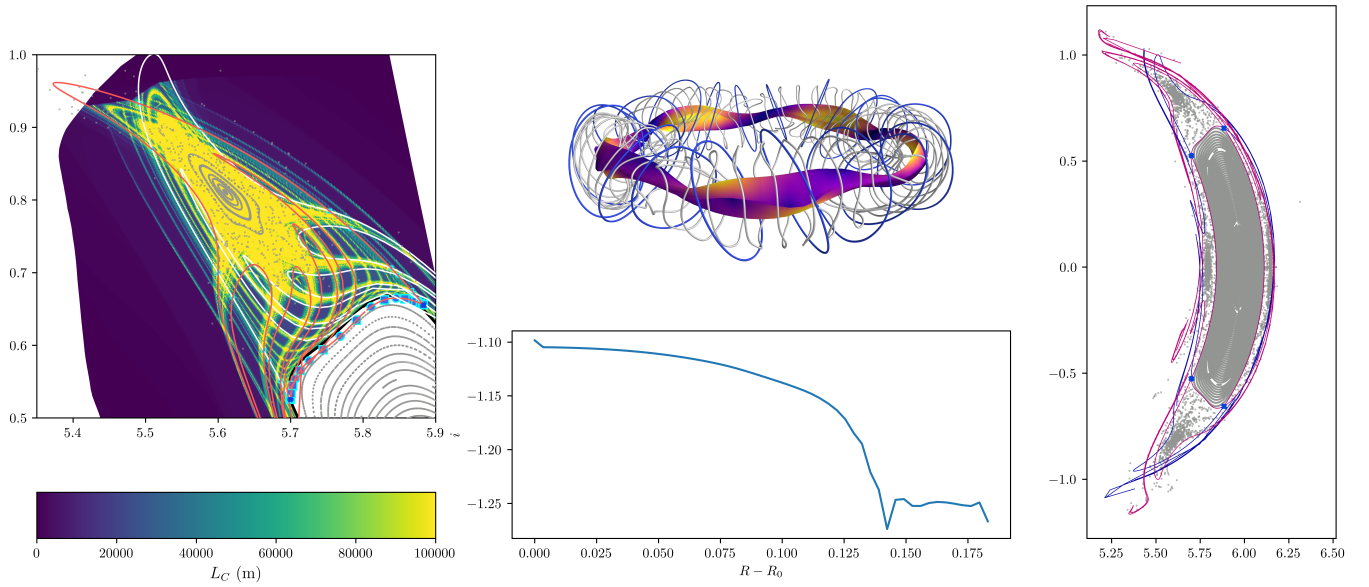


FIG. 10. The W7-X GYM00+1750 configuration. a) Connection length plot showing the minimum distance (both forwards and backwards along field lines) to the wall. Overlaid are the unstable (stable) manifolds of the $5/4$ island chain in white (orange). The features in the connection length plot correlate strongly with the manifolds of the outer heteroclinic connection. The inner heteroclinic connection has a small turnstile area compared to the outer heteroclinic connection. b) Modular coils (white) and planar coils (blue) of the W7-X stellarator, as well as a magnetic surface, colored by the magnetic field strength on it. c) Rotational transform in the GYM configuration. d) Poincaré section of the full $\phi = 0$ cross section, showing nested surfaces inside and a very stochastic edge.

The connection length in the island region is plotted in figure 10 a, and shows a remarkable pattern of alternating long connection length and short connection length regions. The manifolds of the outer heteroclinic connection are also shown on this plot, and there is a strong correlation between the two.

The turnstile mechanism helps to explain how this pattern comes about: the region that is in neither lobe of the first many lobes of the heteroclinic tangle, but is close to the center of the island, has a high likelihood of remaining in that region, and thus has a large connection length. The region that is in one lobe, but not the other, has a probability of hitting the target, but only a fraction of the trajectories in each lobe does. This dark band of low connection length is thus mapped, over and over again, in an ever repeating pattern that Poincaré dubbed a 'trellis'¹⁰, made visible in our analysis of the stellarator divertor!

Just like the QUASR configurations, we again see that the turnstile area on the outer heteroclinic connection is much larger than the turnstile on the inner heteroclinic connection. The oscillations of the inner manifold are not visible at all at this scale of magnification. This means that transport into the island is likely governed by other mechanisms, such as turbulent transport and neoclassical effects.

Plasma that crosses this separatrix is channeled along the stable (unstable) manifold, where it can intersect the wall. The field is so designed that the divertor intersects this stream, and any heat that is transported through the inner turnstile is immediately transported to this wall, and the stochasticity originating from the turnstile on this outer heteroclinic connection is unlikely to have much effect on the heat transport to the

wall.

We have seen in all the stellarator configurations, that on each resonance the turnstile on the outer heteroclinic connection is significantly larger than the turnstile on the inner heteroclinic connection. This is likely because the perturbations that induce the stochasticity are in large part due to ripple effects caused by the finite number of discrete coils. The field lines forming the outer turnstile pass much closer to these coils, and are much more affected.

In terms of stellarator divertor design, it would be interesting to understand if this feature is unavoidable, or just a feature of the configurations analyzed. In other words, would it be possible to generate a field with coils, where the turnstile on the inner separatrix is large, potentially larger than that of the outer separatrix. This could create a stochastic buffer region that could aid in achieving plasma detachment. Configurations such as the GYM00+1750, where the stochasticity is almost completely caused by the interactions of the outer manifolds, do not provide any significant change in the transport from plasma to wall.

VII. CONCLUSIONS AND DISCUSSION

We have illustrated how to use fixed points of the magnetic field line map to analyze chaos and transport in fusion reactor magnetic fields. For this, we have adapted methods used to analyze transport in Hamiltonian dynamical systems to the specific case of analyzing magnetic connectivity in the edge of fusion reactors, by exploiting the mathemati-

cal equivalence between $1\frac{1}{2}$ dimensional Hamiltonian systems and magnetic field line flow in three dimensions. Specifically we have implemented a calculation by Meiss³⁷ based on the action principle to calculate the *turnstile area*, a direct measure for chaotic transport across transport barriers formed by homo- and heteroclinic connections. Such structures are intentionally created in the edge of fusion reactors to control the outflow of heat from the reactor to the vessel wall. We have demonstrated this calculation in the two-dimensional iterated map (the Tokamap), in perturbed axisymmetric fields similar to the tokamak fusion reactor, in fully three-dimensional stellarator fields from the QUASR database and in stochastic configurations of the W7-X fusion reactor.

We have adapted and optimized the calculation for the specific application to three-dimensional magnetic fields, where the integration of field lines is a very costly operation. With the analytical toy model we have shown how different perturbations generate chaotic transport and increase the turnstile area. We have also shown that this calculation is capable of resolving the turnstile area in a very large range of perturbation amplitudes, from very nearly integrable fields, to almost completely stochastic fields.

Transport through an island chain requires a trajectory (field line) to pass through two different turnstiles one after another. The inner turnstile governs passage from the plasma region into the resonance zone, and the outer turnstile then determines passage into the outer chaotic region. If, as in most devices, including the W7-X stellarator, the wall is placed intersecting an edge island, the most important transport channel is through the inner turnstile, as in the island region many trajectories quickly intersect a wall. The calculations of turnstile area in the stellarator configurations show that the outer turnstile area is much larger than the inner turnstile area in the observed configurations. This is likely due to the perturbations due to coil ripple, and the outer manifold passing closer to the coils. Though such fields may look chaotic, the transport from the plasma to the wall is hardly affected by chaos originating from the outer turnstile.

In a fusion reactor, field line flow is not the only factor determining heat transport. It is true that heat conductivity along field lines is several orders of magnitude higher than perpendicular conductivity, but there are other processes that compete. In stellarators there can be significant neoclassical transport⁵², caused by the fact that particle orbits do not follow field lines perfectly. In a stellarator field a significant fraction of particles can lie on orbits that have a net radial displacement, and the net outflow of high-energy particles from the core can cause significant heat transport. Modern optimized stellarators control this by generating fields that minimize such particle orbits, and this has been proven to work in the neoclassically optimized stellarator W7-X⁵². Recently there has also been significant interest in quasisymmetric optimized stellarators, and configurations have been found where nearly all particles are confined⁵⁷.

In an optimized stellarator, where neoclassical transport is very low, turbulent transport becomes the dominant mechanism that transports heat perpendicular to the field lines. This can be caused by a wild array of mechanisms and instabil-

ities including drift waves and charge density oscillations, and a predictive theory of turbulent transport in stellarators is nowhere near. Especially in the edge of the stellarator, where density gradients are large, many instabilities exist, that can compete with direct transport along field lines. Transport caused by direct flow of field lines through the turnstile mechanism is therefore not always the most important factor determining heat transport in the stellarator edge. Especially if the turnstile area is small, it is to be expected that neoclassical or turbulent transport can dominate in this region. The calculation of the turnstile area allows for direct quantification of the amount of transport that is due to stochasticity in the magnetic field, and would allow one to potentially to separate these two transport channels in experiment.

It is important to note that particle trajectories are not identical to field line flow, and especially for high-energy particles the particle trajectories can be misaligned with the magnetic surfaces⁵⁸. Particle motion in three dimensions is governed by its' own three-dimensional Hamiltonian system (with six-dimensional phase space). The dimensionality can be reduced by neglecting the gyromotion (the rapid precession of particles perpendicular to the field), and identifying a spatial coordinate as 'time-like', to yield a four-dimensional Hamiltonian. Chambliss, Paul, and Hudson⁵⁸ brilliantly use this to provide insight into energetic particle transport in stellarators by sectioning this system at specific pitch angles, such that a $1\frac{1}{2}$ -D system is achieved which chaos, islands and resonances can be observed in their two-dimensional sections. It would be interesting to apply turnstile calculations to these reduced-dimensional maps to quantify the rates of energetic particle transport in these sections. Furthermore, transport could be analyzed in the higher-dimensional Hamiltonians without restricting to sections by evaluating the equivalent metrics in the four- or higher dimensional systems.

The calculation of the turnstile area can be applied to a wide range of circumstances, but it still requires user intervention to set up. The fixed points can be found, but choosing the manifolds to trace along and the amount of mappings to use is a process that varies a lot from configuration to configuration. Other approaches, such as level-set learning⁵⁹ could provide a faster and less geometry-specific methods to approach chaos minimization.

The turnstile area also correlates with the stochasticity in the field, and when the turnstile area is zero, the stable and unstable manifold must overlap. The calculation of the turnstile area can be a valuable tool for designing future stellarators, especially when the dynamics on a specific heteroclinic connection (i.e. the inboard or the outboard side of the island) is important for the transport. Using such calculations, the amount of stochasticity in the edge region can be tuned, both on the inner and on the outer turnstile of an island chain. The capability to optimize the turnstile area is in the process of being developed and will be the subject of future publications.

ACKNOWLEDGMENTS

The authors would like to thank Jim Meiss for the inspiring discussions that led to this work about implementing the action calculation in magnetic fields. The authors would like to thank Matt Landreman for invaluable feedback in general, and in particular his suggestions for improving the heteroclinic trajectory finding algorithm. Similarly, our eternal gratitude goes out to Andrew Giuliani for creating and maintaining the QUASR database, which provides a near endless supply of interesting configurations to analyze. This work has been carried out within the framework of the EUROfusion Consortium, partially funded by the European Union via the Euratom Research and Training Programme (Grant Agreement No 101052200 — EUROfusion). The Swiss contribution to this work has been funded by the Swiss State Secretariat for Education, Research and Innovation (SERI). Views and opinions expressed are however those of the author(s) only and do not necessarily reflect those of the European Union, the European Commission or SERI. Neither the European Union nor the European Commission nor SERI can be held responsible for them.

- ¹A. H. Boozer, “Stellarator design,” *Journal of Plasma Physics* **81**, 515810606 (2015).
- ²A. H. Boozer and A. Punjabi, “Simulation of stellarator divertors,” *Physics of Plasmas* **25** (2018).
- ³A. Punjabi and A. Boozer, “Homoclinic tangle in tokamak divertors,” *Physics Letters A* **378**, 2410–2416 (2014).
- ⁴K. Garcia, A. Bader, H. Frerichs, G. Hartwell, J. Schmitt, N. Allen, and O. Schmitz, “Exploration of non-resonant divertor features on the compact toroidal hybrid,” *Nuclear Fusion* **63**, 126043 (2023).
- ⁵A. Bader, B. Faber, J. Schmitt, D. Anderson, M. Drevlak, J. Duff, H. Frerichs, C. Hegna, T. Kruger, M. Landreman, *et al.*, “Advancing the physics basis for quasi-helically symmetric stellarators,” *Journal of Plasma Physics* **86**, 905860506 (2020).
- ⁶P. Morrison, “Magnetic field lines, hamiltonian dynamics, and nontwist systems,” *Physics of Plasmas* **7**, 2279–2289 (2000).
- ⁷D. Kerst, “The influence of errors on plasma-confining magnetic fields,” *Journal of Nuclear Energy. Part C, Plasma Physics, Accelerators, Thermonuclear Research* **4**, 253 (1962).
- ⁸N. Duignan, D. Perrella, and D. Pfefferlé, “Global realisation of magnetic fields as $\frac{1}{2}$ d hamiltonian systems,” *arXiv preprint arXiv:2407.05692* (2024).
- ⁹R. Davies, C. B. Smiet, A. Punjabi, A. Boozer, and S. A. Henneberg, “The topology of non-resonant stellarator divertors,” in preparation (2025).
- ¹⁰H. Poincaré, *Les méthodes nouvelles de la mécanique céleste*, Vol. 2 (Gauthier-Villars et fils, imprimeurs-libraires, 1893).
- ¹¹V. I. Arnol’d, “Small denominators and problems of stability of motion in classical and celestial mechanics,” *Russian Mathematical Surveys* **18**, 85 (1963).
- ¹²J. Moser, “On a nonlinear problem in differential geometry,” in *Dynamical systems* (Elsevier, 1973) pp. 273–280.
- ¹³R. MacKay and J. Meiss, “Relation between quantum and classical thresholds for multiphoton ionization of excited atoms,” *Physical Review A* **37**, 4702 (1988).
- ¹⁴F. A. McRobie and J. M. T. Thompson, “Lobe dynamics and the escape from a potential well,” *Proceedings of the Royal Society of London. Series A: Mathematical and Physical Sciences* **435**, 659–672 (1991).
- ¹⁵S. Naik, F. Lekien, and S. D. Ross, “Computational method for phase space transport with applications to lobe dynamics and rate of escape,” *Regular and Chaotic Dynamics* **22**, 272–297 (2017).
- ¹⁶R. Macay, J. Meiss, and I. Percival, “Transport in hamiltonian systems,” *Physica D: Nonlinear Phenomena* **13**, 55–81 (1984).
- ¹⁷D. Bensimon and L. P. Kadanoff, “Extended chaos and disappearance of kam trajectories,” *Physica D: Nonlinear Phenomena* **13**, 82–89 (1984).
- ¹⁸J. M. Greene, “Two-dimensional measure-preserving mappings,” *Journal of Mathematical Physics* **9**, 760–768 (1968).
- ¹⁹S. Abdullaev, “On mapping models of field lines in a stochastic magnetic field,” *Nuclear Fusion* **44**, S12 (2004).
- ²⁰B. V. Chirikov, “Research concerning the theory of non-linear resonance and stochasticity,” *Tech. Rep. (CM-P00100691, 1971)*.
- ²¹J. M. Greene, “A method for determining a stochastic transition,” *Journal of Mathematical Physics* **20**, 1183–1201 (1979).
- ²²I. Percival, “Variational principles for invariant tori and cantori,” in *Hamiltonian Dynamical Systems* (CRC Press, 2020) pp. 367–375.
- ²³More precisely, a line constant in an S^1 -valued coordinate is mapped to a line that is single-valued in the other coordinate. Equivalently, a map in which each m/n rational orbit (an orbit that traverses the angle coordinate n times for m applications of the map with $n, m \in \mathbb{N}, n \neq 0$) is either part of one continuous family of m/n orbits, only two singular orbits.
- ²⁴S. Aubry, “The twist map, the extended frenkel-kontorova model and the devil’s staircase,” *Physica D: Nonlinear Phenomena* **7**, 240–258 (1983).
- ²⁵J. N. Mather, “Existence of quasi-periodic orbits for twist homeomorphisms of the annulus,” *Topology* **21**, 457–467 (1982).
- ²⁶D. del Castillo-Negrete, J. Greene, and P. Morrison, “Area preserving non-twist maps: periodic orbits and transition to chaos,” *Physica D: Nonlinear Phenomena* **91**, 1–23 (1996).
- ²⁷M. Mugnaine, I. L. Caldas, J. D. Szezech Jr, and R. L. Viana, “Nontwist field line mapping in a tokamak with ergodic magnetic limiter,” *Physical Review E* **108**, 055206 (2023).
- ²⁸R. Balescu, M. Vlad, and F. Spineanu, “Tokamak: A hamiltonian twist map for magnetic field lines in a toroidal geometry,” *Physical Review E* **58**, 951 (1998).
- ²⁹A. Punjabi and A. H. Boozer, “Magnetic turnstiles in nonresonant stellarator divertor,” *Physics of Plasmas* **29** (2022).
- ³⁰A. Giuliani, “Direct stellarator coil design using global optimization: application to a comprehensive exploration of quasi-axisymmetric devices,” *Journal of Plasma Physics* **90**, 905900303 (2024).
- ³¹A. Giuliani, E. Rodríguez, and M. Spivak, “A comprehensive exploration of quasisymmetric stellarators and their coil sets,” *arXiv preprint arXiv:2409.04826* (2024).
- ³²L. E. J. Brouwer, “Über abbildung von mannigfaltigkeiten,” *Mathematische annalen* **71**, 97–115 (1911).
- ³³L. Rais, C. B. Smiet, Z. Qu, and S. R. Hudson, “Pyoculus: A python version of the magnetic field diagnostic package oculus,” (2025).
- ³⁴C. Smiet, G. Kramer, and S. Hudson, “Mapping the sawtooth,” *Plasma Physics and Controlled Fusion* **62**, 025007 (2019).
- ³⁵C. Smiet, G. Kramer, and S. Hudson, “Bifurcations of the magnetic axis and the alternating-hyperbolic sawtooth,” *Nuclear Fusion* **60**, 084005 (2020).
- ³⁶S. Lang, *SI2 (r)*, Vol. 105 (Springer Science & Business Media, 2012).
- ³⁷J. Meiss, “Thirty years of turnstiles and transport,” *Chaos: An Interdisciplinary Journal of Nonlinear Science* **25** (2015).
- ³⁸W. Wei and Y. Liang, “Invariant manifold growth formula in cylindrical coordinates and its application for magnetically confined fusion,” *Plasma Science and Technology* **25**, 095105 (2023).
- ³⁹T. Evans, R. Roeder, J. Carter, B. Rapoport, M. Fenstermacher, and C. Lasnier, “Experimental signatures of homoclinic tangles in poloidally diverted tokamaks,” in *Journal of Physics: Conference Series*, Vol. 7 (IOP Publishing, 2005) p. 174.
- ⁴⁰J. C. Simpson, J. E. Lane, C. D. Immer, and R. C. Youngquist, “Simple analytic expressions for the magnetic field of a circular current loop,” *Tech. Rep.* (2001).
- ⁴¹J. Bradbury, R. Frostig, P. Hawkins, M. J. Johnson, C. Leary, D. MacLaurin, G. Necula, A. Paszke, J. VanderPlas, S. Wanderman-Milne, and Q. Zhang, “JAX: composable transformations of Python+NumPy programs,” (2018).
- ⁴²T. Evans, “Resonant magnetic perturbations of edge-plasmas in toroidal confinement devices,” *Plasma Physics and Controlled Fusion* **57**, 123001 (2015).
- ⁴³I. Joseph, T. Evans, A. Runov, M. Fenstermacher, M. Groth, S. Kasilov, C. Lasnier, R. Moyer, G. Porter, M. Schaffer, *et al.*, “Calculation of stochastic thermal transport due to resonant magnetic perturbations in diii-d,” *Nuclear Fusion* **48**, 045009 (2008).
- ⁴⁴H. Smith, A. Boozer, and P. Helander, “Passive runaway electron suppression in tokamak disruptions,” *Physics of Plasmas* **20** (2013).
- ⁴⁵M. Landreman, B. Medasani, F. Wechsung, A. Giuliani, R. Jorge, and

- C. Zhu, “Simsop: a flexible framework for stellarator optimization,” *Journal of Open Source Software* **6**, 3525 (2021).
- ⁴⁶E. Rodriguez, *Quasisymmetry*, Ph.D. thesis, Princeton University (2022).
- ⁴⁷E. Rodriguez, E. Paul, and A. Bhattacharjee, “Measures of quasisymmetry for stellarators,” *Journal of Plasma Physics* **88**, 905880109 (2022).
- ⁴⁸G. Plunk, “Perturbing an axisymmetric magnetic equilibrium to obtain a quasi-axisymmetric stellarator,” *Journal of Plasma Physics* **86**, 905860409 (2020).
- ⁴⁹S. Henneberg and G. Plunk, “Compact stellarator-tokamak hybrid,” *Physical Review Research* **6**, L022052 (2024).
- ⁵⁰T. S. Pedersen, M. Otte, S. Lazerson, P. Helander, S. Bozhnikov, C. Biedermann, T. Klinger, R. C. Wolf, and H.-S. Bosch, “Confirmation of the topology of the wendelstein 7-x magnetic field to better than 1: 100,000,” *Nature communications* **7**, 13493 (2016).
- ⁵¹A. Dinklage, C. Beidler, P. Helander, G. Fuchert, H. Maaßberg, K. Rahbarnia, T. Sunn Pedersen, Y. Turkin, R. Wolf, A. Alonso, *et al.*, “Magnetic configuration effects on the wendelstein 7-x stellarator,” *Nature Physics* **14**, 855–860 (2018).
- ⁵²C. Beidler, H. Smith, A. Alonso, T. Andreeva, J. Baldzuhn, M. Beurskens, M. Borchardt, S. Bozhnikov, K. J. Brunner, H. Damm, *et al.*, “Demonstration of reduced neoclassical energy transport in wendelstein 7-x,” *Nature* **596**, 221–226 (2021).
- ⁵³There are also five windowpane coils and ten trim coils that can be used to further adjust the field, but do not generate the bulk of the confinement field.
- ⁵⁴Y. Feng *et al.*, “Review of magnetic islands from the divertor perspective and a simplified heat transport model for the island divertor,” *Plasma Physics and Controlled Fusion* **64**, 125012 (2022).
- ⁵⁵Y. Feng, F. Sardei, and J. Kisslinger, “A simple highly accurate field-line mapping technique for three-dimensional monte carlo modeling of plasma edge transport,” *Physics of plasmas* **12** (2005).
- ⁵⁶Y. Gao, Y. Feng, M. Endler, M. W. Jakubowski, J. Geiger, S. Bozhnikov, A. P. Sitjes, F. Pisano, C. P. Dhard, D. Naujoks, *et al.*, “Improvement in the simulation tools for heat distribution predictions and control of baffle and middle divertor loads in wendelstein 7-x,” *Nuclear Fusion* **63**, 026031 (2023).
- ⁵⁷M. Landreman and E. Paul, “Magnetic fields with precise quasisymmetry for plasma confinement,” *Physical Review Letters* **128**, 035001 (2022).
- ⁵⁸A. Chambliss, E. Paul, and S. Hudson, “Fast particle trajectories and integrability in quasisymmetric and quasihelical stellarators,” *arXiv preprint arXiv:2411.04289* (2024).
- ⁵⁹M. Ruth and D. Bindel, “Level set learning for poincaré plots of symplectic maps,” *SIAM Journal on Applied Dynamical Systems* **24**, 611–632 (2025).

Appendix A: vector potential of the toy model field

The toroidal magnetic field B^θ in equation (19) is written in terms of a vector potential. Using gauge freedom, the vector potential is written as a single function A^R . This vector potential is found using mathematica and has the form:

$$A^R = \frac{1}{4r} \text{Real}[(4 \cdot q_a + s \cdot (5r^2 - 10rR + 4R^2 + 2(z - Z)^2)) \cdot \sqrt{-r^2 + 2rR - (z - Z)^2} \cdot (z - Z) - ir(r - 2R) \cdot (4 \cdot q_a + (3r^2 - 6rR + 4R^2) \cdot s) \cdot \log\left(-iz + \sqrt{-r(r - 2R) - (z - Z)^2} + iZ\right)].$$